



Generation of intrinsically CEP stable few-cycle pulses in the mid-IR

Author:

Daniel SÁNCHEZ PEACHAM

Supervisors:

Prof. Dr. Jens BIEGERT (ICFO)

Dr. Michäel HEMMER (ICFO)

Co-supervisor:

Prof. Dr. Christian KOOS (KIT)

MASTER THESIS FOR THE EUROPHOTONICS PROGRAM IN PHOTONICS
ENGINEERING, NANOPHOTONICS AND BIOPHOTONICS

August, 2013



Contents

1	Introduction	2
1.1	Few-cycle pulses in the mid-IR	2
1.2	Motivation for the thesis	2
1.3	Thesis outline	3
2	Theoretical background	4
2.1	The nonlinear wave equation	4
2.2	Difference frequency generation	8
2.2.1	Coupled wave equation	8
2.2.2	Solution to the coupled wave equations	10
2.2.3	Phase matching	11
2.2.4	Non-collinear interaction	13
2.2.5	Intrinsic CEP stability of the DFG process	15
2.3	Numerical modelling of DFG	16
2.3.1	Propagation in linear media	16
2.3.2	Propagation in nonlinear media	17
3	Nonlinear materials for down-conversion to the mid-IR	20
3.1	Review of mid-IR non-linear crystals	20
3.2	Requirements	22
4	Evaluation of analytical solutions	23
4.1	Analytical solutions	23
4.2	Propagation directions and phase matching bandwidth	24
5	Simulations of DFG as an OPCPA seed	28
5.1	Input parameters for the simulations	29
5.2	Target output parameters	30
5.3	Numerical simulation results	31
5.3.1	LGS	32
5.3.2	LGSe	34
5.3.3	LIS	36
5.3.4	CSP	38
5.3.5	AGS	40
5.4	Optimum crystal and configuration	41
5.5	Summary of results	43
6	Experimental characterisation of Tm:Ho system	44
6.1	Spectral and temporal characterisation of the 1.5 μm and 2 μm outputs	44
6.2	Compression of the 2 μm broadband output	46
7	Conclusion and future work	48
A	APPENDIX - SELLMEIER COEFFICIENTS	49
	Bibliography	51

1 Introduction

1.1 Few-cycle pulses in the mid-IR

The development of laser systems in the mid-IR spectral range has attracted a considerable amount of attention in recent years due to multiple scientific, medical, industrial and military applications [1, 2, 3]. In particular, coherent sources capable of producing milli-Joule few-cycle pulses with CEP stability in this spectral region promise to be key-enablers in strong field physics due to ponderomotive scaling of high field physic phenomena such as high harmonic generation (HHG) with wavelength [4, 5].

Direct generation of ultrashort coherent mid-IR radiation, defined in the present work as spanning the wavelength range from 3 to 15 μm , is hindered by the lack of suitable laser media in this spectral range. A few mid-IR gas lasers exist but present narrow band emission which makes them impractical for generation of ultrashort pulses. Solid state lasers, such as those based on Er^{3+} or Cr^{2+} , exhibit an upper limit of about 3 μm . Thus at present the main focus of research into generation of coherent mid-IR radiation is based on parametric down-conversion from the near-IR using nonlinear crystals, where a great number of mature sources exist, specially around 1 μm . Parametric down-conversion can be achieved using a number of techniques, namely difference frequency generation (DFG), optical parametric amplification (OPA), optical parametric generation (OPG) or optical parametric oscillation (OPO). A number of optical parametric chirped pulse amplifier (OPCPA) systems operating in the mid-IR and relying on these techniques have been reported in the last years [6, 7, 8].

1.2 Motivation for the thesis

This work is part of a larger project carried out by the Attoscience and Ultrafast Optics group (AUO) at the Institute of Photonic Sciences (ICFO) to construct an OPCPA laser system capable of delivering CEP stable few-cycle pulses centred at 7 μm wavelength with pulse energies in the milli-Joule range at 100 Hz. The main goal of this thesis is the design of a difference frequency generation (DFG) stage in order to generate a 7 μm seed for the OPCPA chain. The laser providing the broadband pump and signal pulses for the DFG, at 1.55 μm and 2 μm respectively, is a Tm:Ho based fibre laser constructed in collaboration with Menlo Systems. The outputs of laser system relevant to this thesis have been characterised during the project. The DFG stage is a crucial stage in an OPCPA system since CEP stability and bandwidth are both generated in this process and therefore a basic limit on the characteristics of the output of the laser system is set in this process.

1.3 Thesis outline

A brief outline of the thesis is given below:

- Chapter 2: The theoretical aspects regarding the difference frequency generation process are discussed in this chapter. First the analytical solutions predicting the evolution of electric fields involved in the nonlinear interaction are derived from Maxwells equations. Then an alternative theoretical model based on numerical simulations is derived.
- Chapter 3: A brief review of the nonlinear crystals available for parametric down-conversion to the mid-IR is presented. The suitability of the crystals for the system under consideration is discussed and a number of crystals are discarded.
- Chapter 4: The analytical solutions derived in Chap. 2 are numerically evaluated to obtain approximate values for the phase matching angles and phase matching bandwidth.
- Chapter 5: A full 3D nonlinear propagation code based on the numerical model derived in Sec. 2.3 is used to simulate the difference frequency generation stage using the crystals under consideration.
- Chapter 6: The experimental characterisation - performed in the frame of this thesis - of the 1.5 μm and 2 μm broadband outputs from the Tm:Ho laser system is described and a compressor for the 2 μm output is designed and implemented.
- Appendix A: The Sellmeier equations used to model the refractive index of each crystal are gathered for reference.

2 Theoretical background

In the first section of this chapter we give the mathematical notions needed to generally describe nonlinear phenomena. The differential equations that describe the evolution of an electromagnetic field in a nonlinear medium are derived from basic principles. The derivation of the nonlinear wave equation used in the first section can be found in standard nonlinear optics textbooks [10, 11]. In the second section of the chapter, the equations specifically describing difference frequency generation (DFG) are deduced from the results of the first section. In the final section an alternative theoretical model to describe the DFG process based on numerical simulation is presented. This is the numerical model on which the algorithms used by the nonlinear propagation code Sisyfos used for the numerical simulations performed in this thesis are based.

2.1 The nonlinear wave equation

All classical electromagnetic phenomena can be described using Maxwell's equations and the Lorentz force. The former describe how electromagnetic fields are generated and altered by charges, currents and the fields themselves while the latter describes how these fields affect charged particles. In SI units, Maxwell's equations are given by

$$\nabla \cdot \mathbf{D} = \rho / \epsilon_0 \quad (2.1a)$$

$$\nabla \cdot \mathbf{B} = 0 \quad (2.1b)$$

$$\nabla \times \mathbf{E} = \partial_t \mathbf{B} \quad (2.1c)$$

$$\nabla \times \mathbf{H} = \partial_t \mathbf{D} + \mathbf{J}, \quad (2.1d)$$

where \mathbf{E} and \mathbf{B} are the electric and magnetic field vectors, \mathbf{D} is the electric displacement field, \mathbf{H} is the magnetisation field, \mathbf{J} is the current density of free carriers and ρ is the free charge density.

In general, \mathbf{D} and \mathbf{H} are functions of \mathbf{E} and \mathbf{B} known as the constitutive relations, which depend on the medium:

$$\mathbf{D}(\mathbf{r}, t) = f(\mathbf{r}', t', \mathbf{E}, \mathbf{B}) \quad (2.2a)$$

$$\mathbf{H}(\mathbf{r}, t) = g(\mathbf{r}', t', \mathbf{E}, \mathbf{B}), \quad (2.2b)$$

where \mathbf{r}' and t' indicate that the dependence can be non-local and dispersive.

In nearly all cases of interest these relations can be approximated by simple functions.

If the response of the medium to the electromagnetic field is fast and localised, we can assume that \mathbf{H} and \mathbf{D} are determined for a given value of (\mathbf{r}_0, t_0) by specifying $\mathbf{E}(\mathbf{r}_0, t_0)$ and $\mathbf{B}(\mathbf{r}_0, t_0)$. Also, many of the relevant materials in optics are nonmagnetic, such that $\mathbf{H}(\mathbf{r}, t) = \mathbf{B}(\mathbf{r}, t)/\mu_0$. Finally, we assume that \mathbf{E} and \mathbf{D} are related via the polarisation vector \mathbf{P} through the following expression

$$\mathbf{D}(\mathbf{r}, t) = \epsilon_0 \mathbf{E}(\mathbf{r}, t) + \mathbf{P}(\mathbf{r}, t). \quad (2.3)$$

The vector \mathbf{P} (sometimes called the polarisation density to distinguish it from the polarisation of waves) describes the electric field generated by the bound charges in the medium in response to the external electric field \mathbf{E} . Eqn. 2.3 reflects the physical fact that \mathbf{D} and \mathbf{E} are coupled to each other through the interaction with the material medium, given by \mathbf{P} .

Using the constitutive relations shown above and assuming that in the region of interest there are no free charges or currents, a wave equation can be derived from Maxwell's equations by taking the curl of Eqn. 2.1c and introducing the resulting expression into Eqn. 2.1d:

$$\nabla \times \nabla \times \mathbf{E} + \mu_0 \epsilon_0 \partial_t^2 \mathbf{E} = -\mu_0 \partial_t^2 \mathbf{P}. \quad (2.4)$$

The wave equation can be simplified in some situations by expanding the first term using the vector identity $\nabla \times \nabla \times \mathbf{E} = \nabla(\nabla \cdot \mathbf{E}) - \nabla^2 \mathbf{E}$. The first term on the right hand side of the identity is not identically zero due to Eqn. 2.3, but it can be considered to be negligible in many cases. This is specially true in the case of isotropic media and fields with slowly varying envelopes. This approximation reduces the wave equation to the more manageable form:

$$\nabla^2 \mathbf{E} - \mu_0 \epsilon_0 \partial_t^2 \mathbf{E} = \mu_0 \partial_t^2 \mathbf{P}. \quad (2.5)$$

For the more general case that includes non isotropic media and pulses without slowly varying envelopes, the nonlinear wave equation reads

$$\nabla^2 \mathbf{E} - \nabla(\nabla \cdot \mathbf{E}) - \mu_0 \epsilon_0 \partial_t^2 \mathbf{E} = \mu_0 \partial_t^2 \mathbf{P}. \quad (2.6)$$

In order to find how the electromagnetic field evolves in time and space we need to solve Eqn. 2.5 and Eqn. 2.6 for which it is necessary to specify how \mathbf{P} and \mathbf{E} are related. From a physical point of view we want to know how the electric field affects the bound charges in the medium. The simplest model associated to this process is that the external field instantaneously rearranges the charge distribution in the atoms of the medium such that an oscillating dipole moment is induced. The total polarisation is then taken as the average dipole moment per unit volume. For weak electric fields, we expect the charge distribution around the atom to follow the applied electric field such that a linear dependency is established between the induced dipole moment and the applied field, meaning that the atoms will oscillate and radiate at the same frequency as the applied field. In the simplest

case in which the medium is isotropic, the electric field and the polarisation will have the same direction and we can write

$$P(\mathbf{r}, t) = \epsilon_0 \chi E(\mathbf{r}, t), \quad (2.7)$$

where the dimensionless quantity χ is the constant of proportionality between the polarisation and the applied electric field, known as the electric susceptibility. χ related to the refractive index through $n = \sqrt{1 + \chi}$. The free space permittivity ϵ_0 is needed to obtain the correct dimensions ¹.

For stronger fields the response of the system can be rather more complicated, and in general Eqn. 2.7 is insufficient to describe the response of a medium to a laser field. Since \mathbf{P} is computed as an average over the dipole momenta of the atoms forming the medium, there are two possible origins for the nonlinear response of the medium. The first is that the response of the atoms themselves is nonlinear. Using the simple model described above, this can be understood as a nonlinear dependence of the restoring force of the bound charges with displacement. The second is that the number of atoms involved in the interaction (and therefore in the average dipole moment) is dependent on the intensity of the optical field, which is the case for example in a laser medium.

Classical nonlinear optics generally deals with fields that are strong enough for nonlinear effects to be observable but weak enough that photoionization or other high field processes are negligible. In this intermediate regime, called the perturbative regime, we expect the relation between P and E to be linear for small values of E , and to slightly deviate from linearity for larger values. We can expand P as a Taylor series around $E = 0$:

$$P(\mathbf{r}, t) = C_1 E(\mathbf{r}, t) + \frac{1}{2} C_2 E(\mathbf{r}, t)^2 + \frac{1}{6} C_3 E(\mathbf{r}, t)^3 + \dots, \quad (2.8)$$

where the constant C_1 is the first derivative of P with respect to E at $E = 0$, C_2 is the second derivative of P with respect to E at $E = 0$, and so on. By comparison with Eqn. 2.7 we see that $C_1 = \epsilon_0 \chi$. By convention, the polarisation is usually rewritten as:

$$P(\mathbf{r}, t) = \epsilon_0 \chi^{(1)} E(\mathbf{r}, t) + \epsilon_0 \chi^{(2)} E(\mathbf{r}, t)^2 + \epsilon_0 \chi^{(3)} E(\mathbf{r}, t)^3 + \dots, \quad (2.9)$$

where $\chi^{(1)}$ is called the linear susceptibility and $\chi^{(2)}, \chi^{(3)}$ represent the higher order susceptibilities which will characterize the nonlinear response. Note that for simplicity, as in Eqn. 2.7, we have assumed that the medium is isotropic and non-dispersive, such we can take $\chi^{(n)}$ as scalar quantities.

To include dispersion, Eqn. 2.7 and Eqn. 2.9 need to be extended to the case in which the polarisability at t_0 depends not only on the electric field at t_0 , but also on the electric

¹ E , P and ϵ_0 are measured in units of V/m , $C/m^2 = FV/m^2$ and F/m respectively.

field at past times $t < t_0$. This is expressed mathematically as a convolution. For the linear and second order term, which we denote as $P^{(1)}$ and $P^{(2)}$ we get

$$P^{(1)}(\mathbf{r}, t) = \epsilon_0 \int_{-\infty}^t dt' \chi(t') E(\mathbf{r}, t - t') \quad (2.10a)$$

$$P^{(2)}(\mathbf{r}, t) = \epsilon_0 \int_{-\infty}^t dt' \int_{-\infty}^t dt'' \chi(t', t'') E(\mathbf{r}, t - t') E(\mathbf{r}, t - t''), \quad (2.10b)$$

and similarly for $P^{(3)}$, $P^{(4)}$ and so on. The upper integration limit t guarantees causality.

Introducing the dispersive polarisations into the wave equation will lead to a complex expression containing a mix of derivatives and integrals. Fortunately, moving to the frequency domain by taking the Fourier transform will reduce the convolutions to a product:

$$P^{(1)}(\mathbf{r}, \omega) = \epsilon_0 \chi^{(1)}(\omega) E(\mathbf{r}, \omega), \quad P^{(2)}(\mathbf{r}, \omega) = \epsilon_0 \chi^{(2)}(\omega) E(\mathbf{r}, \omega)^2, \quad \dots \quad (2.11)$$

It comes from Eqn. 2.7 and Eqn. 2.9 that in general $\chi^{(n)}$ cannot be invariant under rotations if we need to take into account non-isotropic media or consider the vectorial nature of E and P , like for instance the fact that \mathbf{E} and \mathbf{P} may not be parallel. This leads us to define $\chi^{(n)}$ as tensors of growing order whose components are the constants of proportionality between the polarisation vector and the product of the electric field amplitudes involved in the optical process under consideration. Of particular interest are the second order nonlinear processes, characterized by the second order polarisation. In tensor notation this can be written as

$$\mathbf{P}^{(2)}(\omega_3) = \epsilon_0 \chi^{(2)}(\omega_3, \omega_2, \omega_1) : \mathbf{E}(\omega_1) \mathbf{E}(\omega_2), \quad (2.12)$$

which can be expressed for the i th component of the polarisation as

$$P_i^{(2)}(\omega_3) = \epsilon_0 \sum_{jk} \sum_{perm} \chi^{(2)}(\omega_3, \omega_2, \omega_1) E_j(\omega_1) E_k(\omega_2), \quad (2.13)$$

where ijk refer to the cartesian components of the fields and $perm$ refers to the fact summation is to be performed over all possible permutations of ω_1 and ω_2 such that $\omega_1 + \omega_2 = \omega_3$.

It is mathematically convenient to write the polarisation \mathbf{P} explicitly as the sum of the linear part and the non linear part, $\mathbf{P} = \mathbf{P}^L + \mathbf{P}^{NL} = \epsilon_0 \chi^{(1)} \mathbf{E} + \mathbf{P}^{NL}$. Introducing this into Eqn. 2.5 and defining the relative dielectric constant as $\epsilon_r = \chi^{(1)} + 1$, we obtain the nonlinear wave equation:

$$\nabla^2 \mathbf{E} - \frac{1}{c^2} \partial_t^2 \epsilon_r \mathbf{E} = \frac{1}{\epsilon_0 c^2} \partial_t^2 \mathbf{P}^{NL}. \quad (2.14)$$

if we use the isotropic media approximation from Eqn. 2.5, and

$$\nabla^2 \mathbf{E} - \nabla(\nabla \cdot \mathbf{E}) - \frac{1}{c^2} \partial_t^2 \epsilon_r \mathbf{E} = \frac{1}{\epsilon_0 c^2} \partial_t^2 \mathbf{P}^{NL}. \quad (2.15)$$

if we use the full equation Eqn. 2.6.

2.2 Difference frequency generation

In this section we use the nonlinear wave equation (2.14) deduced in the previous section to describe the nonlinear process of DFG. DFG is a $\chi^{(2)}$ three-wave mixing process in which two optical fields oscillating at $\omega_1 > \omega_2$ are combined in a nonlinear medium to generate a third field at $\omega_3 = \omega_1 - \omega_2$. Energy conservation requires that two photons of frequencies ω_3 and ω_2 be created for every photon of frequency ω_1 that is annihilated. Additionally, momentum conservation imposes the following condition:

$$\mathbf{k}_3 = \mathbf{k}_1 - \mathbf{k}_2, \quad (2.16)$$

which is not intrinsically satisfied and needs to be fulfilled for the process to be efficient. DFG is the basic nonlinear process for parametric down-conversion, in which energy is transferred from a strong optical field ω_1 to a weaker, lower frequency field (which can be ω_3 or ω_2 depending on the situation). For historical reasons, ω_1 and ω_2 are sometimes called the pump and signal, while ω_3 is called the idler. Throughout this work subindexes i, s and p are used to denote the idler, signal and pump fields respectively.

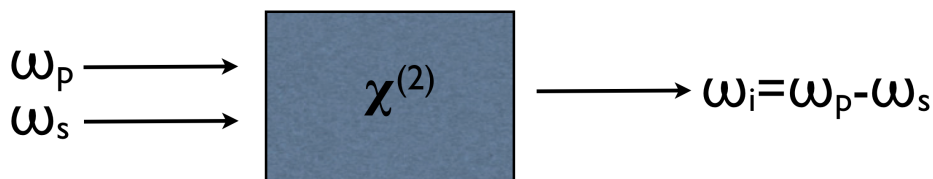


Figure 2.1: Summary of notation used to identify the pump, signal and idler waves throughout this work.

2.2.1 Coupled wave equation

We start from the nonlinear wave equation (2.14). Note that the operators ∇^2 and ∂_t^2 act on each component of the electric and polarisation fields separately, which means that each component satisfies the wave equation independently. Thus for the case of linearly polarised light (which is usually the case in frequency conversion setups) we can reduce to Eqn. 2.14 to a scalar equation. We assume also, without loss of generality, that the propagation is in the z -direction.

For a negligible nonlinear polarisation, the nonlinear wave equation takes a homogenous infinite plane wave as a solution. In particular, for the idler frequency ω_i the electric field

E_i can be expressed using complex notation as

$$E_i(z, t) = A_i e^{i(k_i z - \omega_i t)} + c.c \quad (2.17)$$

where A_i is a constant and $k = n\omega/c$ in order to satisfy the wave equation. It is reasonable to expect that for a small nonlinear polarisation term the solution to the nonlinear wave equation will be similar in form to Eqn. 2.17. We use as a trial solution an infinite plane wave, but we allow the amplitude A_i to vary with the propagation z .

The polarisation term at the idler frequency can also be written as a plane wave $P_i(z, t) = B_i e^{-i(\omega_i t)} + c.c$, where the amplitude B_i is given by Eqn. 2.12. Writing the pump and signal fields as $E_p(z, t) = A_p e^{i(k_p z - \omega_p t)} + c.c$ and $E_s(z, t) = A_s e^{i(k_s z - \omega_s t)} + c.c$ the amplitude of the idler polarisation is

$$B_i = 4\epsilon_0 d_{eff} A_p A_s^* e^{i(k_p - k_s)z}, \quad (2.18)$$

where we have introduced d_{eff} which is the effective nonlinear coefficient defined as $d_{eff} = \chi_{eff}/2$ and χ_{eff} is the scalar value of the 2nd order nonlinear susceptibility for a given polarisation and polarisation directions.

Introducing the plane wave trial solutions for E_i and P_i into the nonlinear wave equation we obtain

$$\left(\partial_z^2 A_i + 2ik_i \partial_z A_i - k_i^2 A_i + \frac{\epsilon(\omega_i)\omega_i^2 A_i}{c^2} \right) e^{ik_i z} = \frac{-4d_{eff}\omega_i^2}{c^2} A_p A_s^* e^{i(k_p - k_s)z}, \quad (2.19)$$

where the complex conjugate terms have been removed and the periodic oscillation term $e^{-i\omega_i t}$ cancels out. Additionally using the fact that $k_i^2 = \epsilon(\omega_i)\omega_i^2/c^2$, the third and fourth term on the left hand side of the equation cancel out. Multiplying on both sides by $e^{-ik_i z}$ we obtain

$$\partial_z^2 A_i + 2ik_i \partial_z A_i = \frac{-4d_{eff}\omega_i^2}{c^2} A_p A_s^* e^{i(k_p - k_i - k_s)z}. \quad (2.20)$$

A further approximation is often used at this point which consists of neglecting the term containing the second derivative on the left hand side of the equation. This is known as the slowly varying amplitude approximation and is equivalent to assuming that the amplitude term A_i varies little over a distance equal to one optical cycle. Since the energy transfer between the fields is usually only relevant after a propagation much longer than one optical cycle, the approximation leads to valid results in most cases. Surprisingly, the approximation is even accurate for pulses in the few cycle regime. Mathematically, this condition is expressed as $|\partial_z^2 A_i| \ll |k_i \partial_z A_i|$. The resulting differential equation becomes

$$\partial_z A_i = \frac{2id_{eff}\omega_i^2}{k_i c^2} A_p A_s^* e^{i\Delta k z}, \quad (2.21)$$

where the term Δk is known as the phase mismatch and is defined as $\Delta k = k_p - k_s - k_i$. We

can obtain analogous equations for the pump and signal fields:

$$\partial_z A_p = \frac{2id_{eff}\omega_p^2}{k_p c^2} A_s A_i e^{-i\Delta k z} \quad (2.22a)$$

$$\partial_z A_s = \frac{2id_{eff}\omega_s^2}{k_s c^2} A_i^* A_p e^{i\Delta k z} \quad (2.22b)$$

Eqn. 2.21 and Eqn. 2.22 are known as the coupled wave equations and solving them for the appropriate boundary conditions will give us the evolution of the fields involved in the nonlinear interaction.

2.2.2 Solution to the coupled wave equations

The general solution for the coupled wave equation was derived in 1962 by Armstrong *et al.* [12] and confirmed experimentally in 1979 by Baumgartner *et al.* [13]. The derivation of the full solution is rather involved and beyond the scope of this work. We can obtain a useful physical picture of the nonlinear process by making the simplifying assumption that the conversion efficiency is low and the signal and pump fields are constant throughout the nonlinear process. In this case the amplitude of the idler field at an arbitrary propagation length l can be found by integrating Eqn. 2.21:

$$A_i(l) = \frac{2id_{eff}\omega_i^2 A_p A_s}{k_i c^2} \int_0^l e^{i\Delta k z} dz = \frac{2id_{eff}\omega_i^2 l^2 A_p A_s}{k_i c^2} \left(\frac{e^{i\Delta k l} - 1}{i\Delta k} \right) \quad (2.23)$$

The corresponding intensities can be found by computing $I = 2n\epsilon_0 c |A|^2$. We obtain the intensity of the idler after an arbitrary propagation distance of l

$$I_i = I_p I_s \left(\frac{2d_{eff}\omega_i^2 l^2}{k_i c^2} \right)^2 \text{sinc}^2(\Delta k l) \quad (2.24)$$

Even though Eqn. 2.24 is derived using simple and unphysical assumptions, the equation gives some useful insight and is worth analysing. The first two terms are the contributions given by the pump and signal peak intensities. This points to the rather intuitive fact that the nonlinear process is driven by the intensity of the input fields. The next term accounts for most of the material parameters involved, and most importantly it shows that the idler intensity is proportional to the square of both d_{eff} and the propagation distance. Finally, the last term accounts for the phase mismatch Δk through a modulating term given by the square of a sinc function. This term is known as the phase mismatch factor and is plotted in Fig. 2.2. For $\Delta k = 0$, which is known for perfect phase matching, the sinc function has a value of 1, and in this case the idler intensity is a quadratic function of propagation distance. For $\Delta k \neq 0$ however, there is dramatic decrease in efficiency as the sinc functions drops for increasing values of Δk down to zero at $\Delta k l / 2 = \pi$, and then oscillates around decreasingly

small values. The fact that the propagation distance is also found in the phase mismatch factor means that the phase mismatch increases with propagation distance.

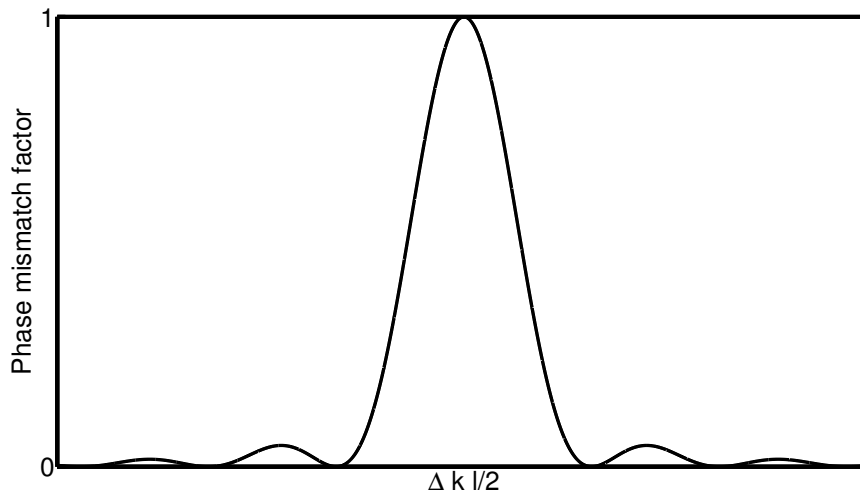


Figure 2.2: Phase mismatch factor

The general solution for the coupled wave equation given by Armstrong *et al.* is complex and provides little physical insight. Nevertheless the special case in which the pump field is undepleted and there is no applied idler field gives the following useful expression for the pump, signal and idler intensities

$$I(\omega_i, l) = \frac{\omega_i}{\omega_s} I(\omega_s, l = 0) \cdot \sinh^2(lg), \quad (2.25a)$$

$$I(\omega_s, l) = I(\omega_s, l = 0) \cdot \cosh^2(lg), \quad (2.25b)$$

$$I(\omega_p, l) = I(\omega_p, 0), \quad (2.25c)$$

where g is the parametric gain, given by:

$$g = \left(d_{eff}^2 \frac{2\omega_s\omega_i I(\omega_p)}{c^3 \epsilon_0 n(\omega_p) n(\omega_s) n(\omega_i)} - \left(\frac{\Delta k}{2} \right)^2 \right)^{1/2}. \quad (2.26)$$

Even though formally Eqn. 2.24 and Eqn. 2.25a are very different, it can readily be observed that they follow the same dependence with phase mismatch factor, which acts as a modulating factor determining the efficiency of the process.

2.2.3 Phase matching

As can be seen from Eqn. 2.24 and Eqn. 2.25, in a nonlinear mixing process the efficiency of the energy exchange depends crucially on the phase mismatch Δk . This can be explained in terms of phase. It can be shown [14] that the highest conversion efficiency from

the pump to the signal and idler fields is found when the relative phase of the three waves is $\phi = \Phi_p - \Phi_s - \Phi_i = -\pi/2$, where Φ_p , Φ_s and Φ_i are the phase of the pump, signal and idler. For increasing values of ϕ the efficiency of the process is reduced until reaching $\phi = 0$ when back conversion occurs and energy is transferred from the idler and signal back to the pump field.

When no idler field is applied at the input, the generated idler phase at $z \approx 0$ automatically takes the value $\Phi_i = \Phi_p - \Phi_s + \pi/2$. As the nonlinear process couples the evolution of the fields, the idler phase will evolve according to [14]

$$\Phi_i = \Phi_p - \Phi_s + \frac{\pi}{2} - \frac{\Delta k z}{2}. \quad (2.27)$$

This means that for $\Delta k = 0$ the phase relationship between the fields is fixed and the conversion efficiency is a maximum throughout the interaction while for $\Delta k \neq 0$ the conversion efficiency will decrease with propagation distance until back conversion is reached after a certain distance. Thus, the objective is to minimise Δk , which is known as phase matching.

Several experimental techniques exist to achieve phase matching. They can be understood by considering the simple case of collinear interaction, where the wave vectors of the three waves are parallel. In this case the phase matching condition $\Delta k = 0$ can be written as

$$\omega_p n(\omega_p) = \omega_s n(\omega_s) + \omega_i n(\omega_i). \quad (2.28)$$

In principle this condition can be achieved in some specific cases through use of anomalous dispersion only. In practice though, the most common way of achieving phase matching is by making use of the birefringence displayed by many nonlinear materials. A birefringent crystal exhibits a different refractive index for different polarisations. Phase matching can be achieved through use of this property by choosing the polarisation of the input fields such that the phase matching condition is fulfilled.

In a uniaxial crystal, light polarised perpendicular to the plane containing \mathbf{k} and the optical axis is known as the ordinary ray as it experiences a refractive index n_o while light that is polarised in the plane containing \mathbf{k} and the optical axis is known as the extraordinary ray and experience a refractive index n_e . The geometrical configuration can be seen in Fig. 2.3. Additionally, the refractive index of the extraordinary ray depends on the angle that it forms with the optical axis according to

$$\frac{1}{n_e^2} = \frac{\sin^2 \theta}{n_e^2} + \frac{\cos^2 \theta}{n_o^2} \quad (2.29)$$

where n_e is the refractive index of the extraordinary wave when $\theta = 90^\circ$. In a biaxial crystal, the situation is similar but less straightforward since there are two optical axis in this case

and it only makes sense to speak of ordinary and extraordinary rays when propagation is one of the principle planes of the crystal.

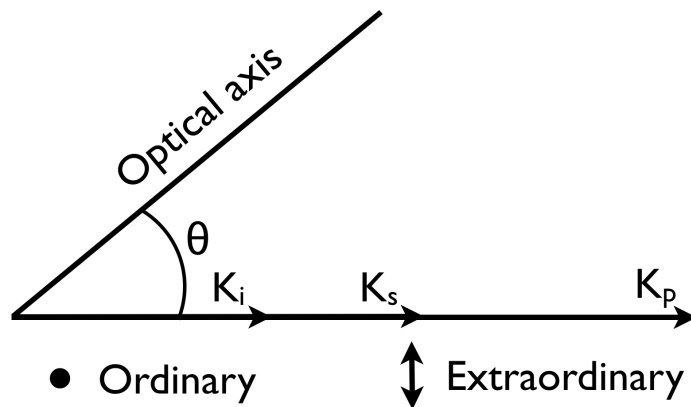


Figure 2.3: Configuration of beam geometry in collinear interaction.

In order for the phase matching condition to be fulfilled, the high frequency field must be polarised such that it experiences the lower of the two refractive indices. In a negative uniaxial crystal this corresponds to the extraordinary ray, while in a positive uniaxial crystal it corresponds to the ordinary ray. It still remains to set the polarisation of the lower frequency waves. If the two waves are polarised parallel with respect to each other, this is known as Type I phase matching. In a negative uniaxial crystal for example, the signal and idler would both be ordinary rays. If the two lower frequency waves are orthogonal, this is known as type II phase matching. In a negative uniaxial crystal, this would mean that depending on the dispersion of the material either the idler or the signal would be the extraordinary ray. Experimentally, fine tuning of the refractive indices is achieved through use of the angle dependence of n_e given in Eqn. 2.29.

2.2.4 Non-collinear interaction

A different phase matching arrangement which is gaining widespread use when dealing with broadband pulses known as noncollinear geometry [15, 16]. The technique involves introducing an angle between the input beams such that a different angle is formed between the optical axis and the pump and signal. In this work it is assumed by convention that the signal beam is perpendicular to the input facet of the crystal while the pump beam is tilted at an angle. All the angles refer to internal angles inside the crystal unless otherwise stated. The angle between the signal and the optical axis is known as the propagation angle and is represented by θ . The angle formed between the pump and the signal is called the noncollinear angle and represented by α . Thus the pump propagates at an angle $\theta + \alpha$ from the optical axis. The angle between the idler and the optical axis is represented by β . The geometrical setup is shown in Fig. 2.4.

By using noncollinear geometry we increase our freedom to orientate the crystal. In

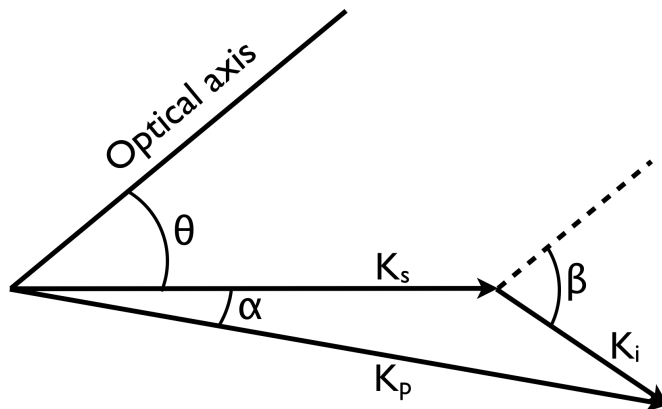


Figure 2.4: Configuration of beam geometry in noncollinear interaction.

collinear geometry, the phase matching condition is fulfilled for a fixed value of θ while for noncollinear geometry we obtain a set of pairs of values (α, θ) . This means that we can choose (α, θ) to maximise a given property of the crystal. Typically for broadband pulses, this freedom is used to reduce the group velocity mismatch (GVM) which limits the temporal overlap of the pulses in the time domain and the width of the phase matched spectral range in frequency domain. This can be done by minimising

$$GVM = \frac{1}{v_{g,p}} - \frac{1}{v_{g,s}} = \frac{\partial k_p}{\partial \omega}|_{k_{p,0}} - \frac{\partial k_s}{\partial \omega}|_{k_{s,0}}, \quad (2.30)$$

where $v_{g,p}$ and $v_{g,s}$ are the pump and signal group velocities and $k_{p,0}$ and $k_{s,0}$ are the wave vectors at the central frequency of the pump and signal respectively. Since k_p and k_s depend on the refractive index, tuning the angle such that phase matching is achieved and GVM is minimised is possible. In the context of short pulses, GVM leads to the effect of temporal walkoff and is a serious limiting factor of conversion efficiency. When broadband phase matching is not an issue, the extra degree of freedom can be used to obtain a higher nonlinearity through the dependence of the value of d_{eff} with angle.

In some cases noncollinear geometry can be used to increase the interaction length by compensating the effect of a phenomenon known as spatial walkoff. Spatial walkoff occurs for the extraordinary beam in birefringent media and leads to an angle being formed between the Poynting vector and the propagation direction. It can be calculated using the following expression

$$\rho = -\frac{1}{n_e} \frac{\partial n_e}{\partial \theta} \quad (2.31)$$

In practice it limits the interaction length of the two pulses by decreasing the spatial overlap. This effect can be reduced by using a noncollinear angle that compensates for the walkoff effect. In general, we have freedom to choose α such that this occurs.

Finally, we point that in noncollinear geometry the phase mismatch $\Delta \mathbf{k}$ needs to be

considered as a vector and can be decomposed into a transverse and longitudinal term such that $\Delta \mathbf{k} = \Delta \mathbf{k}_{\parallel} + \Delta \mathbf{k}_{\perp}$. Here the transverse and longitudinal components are taken with respect to the signal. As an example, for Type I phase matching in a negative uniaxial ($n_e < n_o$) crystal and assuming the geometrical configuration shown in Fig. 2.4, the general noncollinear phase mismatch is given by

$$\Delta k_{\parallel} = \frac{\omega_p n_e(\omega_p, \theta + \alpha)}{c} \cos(\alpha) - \frac{\omega_s n_o(\omega_s)}{c} - \frac{\omega_i n_o(\omega_i)}{c} \cos(\beta) \quad (2.32a)$$

$$\Delta k_{\perp} = \frac{\omega_p n_e(\omega_p, \theta + \alpha)}{c} \sin(\alpha) - \frac{\omega_i n_o(\omega_i)}{c} \sin(\beta) \quad (2.32b)$$

The collinear case is obtained by setting $\alpha = 0$. For a positive uniaxial ($n_e > n_o$) crystal n_e and n_o need to be exchanged.

2.2.5 Intrinsic CEP stability of the DFG process

The ability to deliver carrier-envelope phase (CEP) stable pulses is a pre-requisite for femtosecond oscillators intended for use in strong field physics experiments [17, 18]. Control of CEP is one of the key features in state-of-the-art femtosecond laser systems. There are a number of techniques available to actively detect and correct CEP drift. In systems using traditional gain media, such as Ti:Sapphire laser systems, most of these techniques operate by using one or multiple feedback loop setups in which the CEP drift is measured and actively compensated for in the laser cavity by modulating the pump power or driving an acousto-optic modulator [19, 20]. Optical parametric amplification is in principle a CEP preserving process, and therefore if CEP stable pulses are seeded in an OPA chain operated in the non-depletion regime, amplified CEP stable pulses are expected at the output of the chain. In practice though, time jitter between the seed and pump pulses can lead to CEP instabilities. Therefore in an OPCPA system, specially when broadband amplification is required, active synchronisation of the pump and seed pulses is required in both the DFG and OPA stages. In both cases, active CEP control requires the use of complex timing stabilisation mechanisms that add complexity and cost to the system.

A simple scheme for obtaining intrinsically CEP stable pulses from the DFG stage is explained in the following. The key to this technique is that the pump and signal pulses are generated in a single cavity, which is the case of the Tm:Ho fibre system under consideration. The main idea can be understood by considering the spectrum of a mode-locked cavity as shown in Fig. 2.5. $\Delta\omega$ is the spacing between the modes, which is given by the repetition rate, while ω_{offset} is a frequency offset which suffers small random fluctuations. This fluctuation in frequency domain leads to CEP instabilities in time domain. We assume for simplicity that the pump and signal are monochromatic. The frequency of the pump and signal are then

given by:

$$\omega_p = N\Delta\omega + \omega_{\text{offset}} \quad (2.33a)$$

$$\omega_s = M\Delta\omega + \omega_{\text{offset}}, \quad (2.33b)$$

where N and M are arbitrary integers determining the pump and signal frequencies such that $N > M$. According to the DFG process, the generated idler frequency can be found by taking the difference of two input pulses

$$\omega_i = N\Delta\omega + \omega_{\text{offset}} - (M\Delta\omega + \omega_{\text{offset}}) \quad (2.34a)$$

$$= \Delta\omega(N - M), \quad (2.34b)$$

where the random fluctuation term ω_{offset} has cancelled out. Thus in this system the fact that the pump and signal come from the same mode-locked oscillator leads to intrinsic CEP stable idler pulses without requiring active stabilisation.

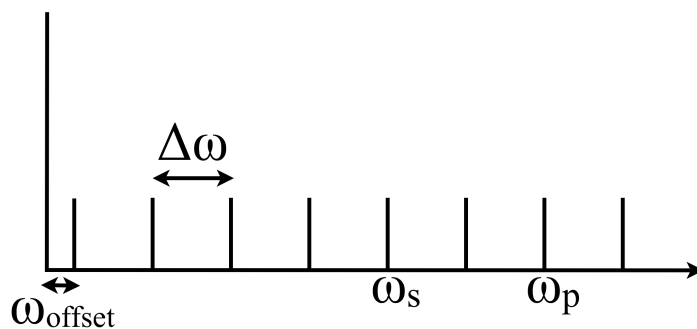


Figure 2.5: Spectrum of a mode locked laser showing the pump and signal modes.

2.3 Numerical modelling of DFG

In this section the theory underlying the numerical model used by the nonlinear propagation code Sisyfos is explained [21]. For simplicity, we assume that the fields are linearly polarised and consider only one polarisation mode.

2.3.1 Propagation in linear media

We start by considering the representation of the electric field as a plane wave solution of the wave equation in free space.

$$\mathbf{E}(x, y, z, t) = A\mathbf{e}e^{-i(\omega_i t + \mathbf{k} \cdot \mathbf{r})} + c.c., \quad (2.35)$$

where A is a complex constant, \mathbf{k} is the wave vector and \mathbf{e} gives the polarisation. We define the propagation direction as the unit vector \mathbf{e}_k such that $\mathbf{k} = k\mathbf{e}_k$. Note that in free space \mathbf{k}

and \mathbf{e} are orthogonal due to the constraint $\nabla \cdot \mathbf{E} = 0$.

The propagation equations for the electromagnetic field can either be solved in time-space or frequency domain. Each domain has its own advantages depending on the approximations that are required. In the case of broadband pulses, working in frequency domain allows to easily account for dispersion exactly, while in time-space domain \mathbf{k} has to be expanded as a truncated Taylor series and convergence is not guaranteed for wide spectra. Additionally, as is discussed in the following section, the slowly varying amplitude approximation is less restrictive in spectral domain than in time. For these reasons Sisyfos computes propagation in frequency domain.

If the real electric field at $z = 0$ is given by $\mathbf{E}(x, y, 0, t)$ the spectral modes $\mathcal{E}(k_x, k_y, \omega)$ can be computed by making use of the Fourier transform:

$$\mathcal{E}(k_x, k_y, \omega) = \frac{1}{(2\pi)^3} \int \int \int_{-\infty}^{\infty} \mathbf{E}(x, y, 0, t) \cdot \mathbf{e}(k_x, k_y) e^{-i(\omega t - k_x x - k_y y)} dx dy dt + c.c. \quad (2.36)$$

Assuming that the real electric field is forward propagating ($k_z > 0$), in the case of free space the complex electric field vector $\mathbf{E}(x, y, z, t)$ can be reconstructed at $z \neq 0$ by computing

$$\mathbf{E}(x, y, z, t) = \int_0^{\infty} \int \int_{-\infty}^{\infty} \mathcal{E}(k_x, k_y, \omega) \mathbf{e}(k_x, k_y) e^{-i(\omega t - \mathbf{k} \cdot \mathbf{r})} dk_x dk_y d\omega + c.c., \quad (2.37)$$

where $k_z = (\omega^2/c^2 - k_x^2 - k_y^2)^{1/2}$ and the positive integration limits correspond to ω .

In the case of linear dielectric media the index of refraction must be included in the computation of the wave vectors such that $k_z = (\omega^2 n^2/c^2 - k_x^2 - k_y^2)^{1/2}$. It can be shown by introducing a trial plane wave solution into the wave equation that in general in dielectric media for a given propagation direction, which is determined by \mathbf{e}_k there are two electric fields with orthogonal polarisation that satisfy the equation. In the case of birefringent media the two fields experience different refractive indices depending on their polarisation. Thus in general the refractive index of an electric field in dielectric media depends on its frequency (which accounts for dispersion), propagation direction (which accounts for non isotropic media) and polarisation state (which accounts for birefringence). Eqn. 2.36 and Eqn. 2.37 can still be used as propagation equations in the case of linear media but the refractive index must include the dependencies described above. Note that this dependance is also implicitly contained in the polarisation vector \mathbf{e} .

2.3.2 Propagation in nonlinear media

When considering the effect of nonlinear dielectric media, the nonlinear wave equation 2.15 must be used. We point out that Sisyfos uses the full nonlinear wave equation. We

assume that the propagation equations given above are still valid but now expect the spectral modes to vary with z . Thus the electric field in time domain will now be obtained through

$$\mathbf{E}(x, y, z, t) = \int_0^\infty \int \int_{-\infty}^\infty \mathcal{E}(k_x, k_y, \omega, z) \mathbf{e}(k_x, k_y, \omega) e^{-i(\omega t - \mathbf{k} \cdot \mathbf{r})} dk_x dk_y d\omega + c.c., \quad (2.38)$$

where the only difference with the case of linear media is the dependance of the spectral modes with propagation distance.

The nonlinear polarisation term \mathbf{P}_{NL} can also be expressed in frequency domain by using the Fourier transform:

$$\mathbf{P}_{NL}(x, y, z, t) = \int_0^\infty \int \int_{-\infty}^\infty \mathbf{p}(k_x, k_y, \omega, z) e^{-i(\omega t - \mathbf{k} \cdot \mathbf{r})} dk_x dk_y d\omega + c.c., \quad (2.39)$$

where $\mathbf{p}(k_x, k_y, \omega, z)$ are the nonlinear polarisation spectral modes.

Once we have the trial solutions for \mathbf{E} and \mathbf{P}_{NL} , the terms $\nabla^2 \mathbf{E}$, $\nabla \cdot \mathbf{E}$, $\nabla(\nabla \cdot \mathbf{E})$, $\partial_t^2 \mathbf{E}$ and $\partial_t^2 \mathbf{P}_{NL}$ can be computed and inserted into the nonlinear wave equation. After some basic algebraic manipulations we obtain

$$e^{ik_z z} (2ik_z (\partial_z \mathcal{E} \mathbf{e}) - ik (\partial_z \mathcal{E}) (e_z \mathbf{e}_k - \sin(\rho) z)) = -\mu_0 \omega^2 \mathbf{p}, \quad (2.40)$$

where e_z is the z -component of the polarisation vector \mathbf{e} and we have introduced walkoff angle $\rho = \mathbf{e} \cdot \mathbf{e}_k$, which is the angle between the Poynting vector (which is perpendicular to the polarisation vector \mathbf{e}) and the propagation direction \mathbf{e}_k . We have neglected second order derivatives of \mathcal{E} using the slowly varying amplitude approximation in spectral domain. This is less restrictive than the equivalent approximation in time domain, since it requires the spectral amplitudes to vary slowly over an optical cycle while no restriction is imposed on the pulse length or dispersion of the real electric. The equation above can be simplified by neglecting the second term on the left hand side. This is a small approximation since the propagation is mainly in the z -direction while the polarisation is nearly perpendicular to \mathbf{k} , which means that the z -component of the polarisation e_z must necessarily be small. The third term can also be neglected since the walkoff angle is also small. Using these approximations we find the propagation equation in nonlinear media:

$$\partial_z \mathcal{E} = i \frac{\mu_0 \omega^2 \mathbf{p} \cdot \mathbf{e}}{2k_z} e^{-ik_z z} = i \frac{\mu_0 c \omega \mathbf{p} \cdot \mathbf{e}}{2n} e^{-ik_z z} \quad (2.41)$$

where the approximation $k_z \approx |k| = \omega n / c$ was used.

In order to take into account the absorption, the amplitude \mathcal{E} are defined such that they include absorption coefficient α :

$$\mathcal{A} = \mathcal{E} e^{-\alpha/2}, \quad (2.42)$$

This is convenient for Sisyfos since the typical absorption length is much longer than the wavelength and therefore including α requires little additional computation. Substituting the expression for \mathcal{E} into the definition of \mathcal{A} leads to the continuous version of the discrete propagation equation that Sisyfos actually solves for each of the beams involved in the nonlinear interaction.

$$\partial_z \mathcal{A} = -\frac{\alpha}{2} \mathcal{A} + i \frac{\mu_0 c \omega \mathbf{P} \cdot \mathbf{e}}{2n} e^{-ik_z z} \quad (2.43)$$

The discrete version of this equation can be sent directly to an ordinary differential equation (ODE) solver. For the simulations undertaken for the present work, a Runge-Kutta ODE solver with adaptive step was used.

Finally, it remains to specify the nonlinear polarisation term. At present Sisyfos support 2nd order polarisation, nonlinear refractive index, 2-photon absorption and thermo optic effects. \mathbf{P}_{NL} is defined for each beam m as

$$\begin{aligned} \mathbf{P}_{NL,m}(x, y, z, t) = & \epsilon_0 \sum_{rs} \chi_{mrs}^{(2)} \mathbf{E}_r \mathbf{E}_s \\ & + 2n_m \epsilon_0 \left(\mathbf{E}_m \sum_r n_{2,mr} I_r + i \mathbf{E}_m \sum_r \beta_{mr} I_r + \mathbf{E}_m \Delta n(x, y, z) \right), \end{aligned} \quad (2.44)$$

where $\chi_{mrs}^{(2)}$ is the second order susceptibility tensor for the interaction between the beams m, r, s and is considered to be constant over the bandwidth of each beam. The second term contains the intensity dependent refractive index which accounts for cross- and self-modulation. The third term is the two-photon absorption (TPA) where $\beta\omega/c$ is the TPA coefficient while the last term represent the spatial varying refractive index due to thermal effects.

3 Nonlinear materials for down-conversion to the mid-IR

The feasibility of the down-conversion process is determined by the choice of nonlinear media, which must exhibit a set of unique properties such as transparency at the pump, signal and idler wavelengths, phase matching abilities via birefringence or quasi-phase matching, high damage threshold, ease of growth that guarantees samples of good quality and commercial availability. Oxide nonlinear crystal, for which there exists a well-established growth technology, are limited in transparency range to 4 or 5 μm in the best case due to intrinsic multiphonon absorption. Therefore non-oxide materials such as binary and ternary non-centrosymmetrics inorganic crystals must be used. In general these materials require more complex growth process than oxides, which leads to an increase in growth defects and corresponding residual losses. Nevertheless over the last two decades an intensive search for new nonlinear materials suitable for downconversion to the mid-IR has lead to an improvement on existing crystals as well as on the synthesis of promising new materials [9]. In this section we first present a brief review of the nonlinear crystals suitable for down-conversion to the mid-IR. Then we select those crystals with the appropriate characteristics for a DFG stage pumped with broadband pulses at 1.55 μm and 2 μm .

3.1 Review of mid-IR non-linear crystals

A list of the available nonlinear crystals featuring both transparency in the mid-IR and phase matching abilities is shown in Tab. 3.1. The two first crystals on the list, proustite (AgAsS_3 or AAS) and pyrargyrite (AsSbS_3 or ASS) showed some initial promise and were used for nonlinear frequency conversion [22], but during the 1980's were replaced by other crystals due to growth issues and low damage threshold. Silver thiogallate (AgGaS_2 or AGS) and silver gallium selenide (AgGaSe_2 or AGSe) are negative uniaxial semiconductor chalcopyrite that have been widely used for downconversion to the mid-IR [23, 24]. Their relatively large band gap allows them to be pumped at 1 μm without two photon absorption (TPA) and, in the case of AGSe, the transparency reaches beyond 15 μm and can be used for up-conversion of CO_2 laser radiation [25]. Both AGSe and AGS have low thermal conductivity and damage threshold, making them unsuitable for high power application with fs lasers.

Zinc germanium phosphide (ZnGeP_2 or ZGP) and cadmium germanium arsenide (CdGeAs or CGA) are positive uniaxial chalcopyrite showing extremely high nonlinearity [26]. ZGP also presents good thermal conductivity and damage threshold but residual and multiphonon absorption limit the transparency range and the pump wavelength must lie above 2 μm to

avoid TPA. Nevertheless ZGP is one of the most widely used crystal for down conversion to the mid-IR region [27, 28]. For CGA, values of d_{eff} as high as 185 pm/V have been reported [29], but good optical qualities are difficult to obtain and the lower wavelength limit is even higher than for ZGP. This makes these two crystal unsuitable for pumping at 1 μ m.

Cadmium selenide (CdSe) has modest nonlinearity and low birefringence which means that phase matching can be issue [30]. Gallium selenide (GaSe or GS) has a large nonlinearity and birefringence but a very low damage threshold. In addition it is an extremely soft crystal (0 on the Mohs hardness scale) making it difficult to polish and it has a structure such that it can only be cut perpendicular to the optical axis, making certain phase matching configuration unattainable [31].

Tin hypthiodiphosphate (SnP_2S_6 or SPS) and thallium arsenic selenide (Tl_3AsSe_3 or TAS) are considered to be exotic nonlinear crystals [32, 33]. SPS presents a phase transition to a centrosymmetric structure at low temperature, while TAS has extremely low thermal conductivity. AgGaGeS_4 is what is known as a mixed crystal [34]. These crystals are created by doping a ternary compound to obtain more complex quaternary compounds. In this case AGS is doped with GaS to obtain a new biaxial crystal. These crystals present serious growth problems, and interest in them is declining.

Mercury thiogallate (HgGa_2S_4 or HGS) and cadmium silica phosphate (CdSiP_2 or CSP) are both very promising new uniaxial chalcopyrites that have drawn attention recently. HGS was originally developed in the 1970's [35] but growth problems limited the optical quality. It presents a nonlinearity as high as AGS with a much higher damage threshold. The fabrication process has been greatly improved in the past decades and some practical application have been demonstrated [36]. CSP has a very high nonlinearity [37], $d_{eff} = 85$ pm/V and can be pumped without two photon absorption at 1 μ m, but low damage threshold limits its application in high power systems.

The four ternary wide band-gap biaxial crystal LiGaS_2 (LGS), LiGaSe_2 (LGSe), LiInS_2 (LIS) and LiInSe_2 (LISE) are relatively new additions to the list [38, 39, 40]. Although LGS was reported as early as 1947, and poor quality sample of LIS were studied in the 1970s, growth related problems prevented proper characterisation of these crystals until the last decade. They present the lowest nonlinearity of all the crystals considered here, around an order of magnitude less than CSP for instance. On the other hand, their wide band gap allows them to be directly pumped at 800 nm with fs lasers without TPA. In addition their thermal properties and damage threshold are also improved with respect to the other mid-IR crystals such as AGS and GS.

Crystal	Type	Transparency range [nm]
AgAsS ₃ (AAS)	Neg. uniaxial	600-13000
AsSbS ₃ (ASS)	Neg. uniaxial	700-14000
AgGaS ₂ (AGS)	Neg. uniaxial	500-13000
AgGaSe ₂ (AGSe)	Neg. uniaxial	710-18000
ZnGeP ₂ (ZGP)	Neg. Uniaxial	2000-11000
CdGeAs (CGA)	Pos. uniaxial	2400-18000
CdSe (CS)	Pos. Uniaxial	750-20000
GaSe (GS)	Neg. uniaxial	650-18000
SnP ₂ S ₆ (SPS)	Biaxial	530-8000
Tl ₃ AsSe ₃ (TAS)	Neg. uniaxial	1250-2000
AgGaGeS ₄ (AGGS)	Biaxial	700-13000
CdSiP ₂ (CSP)	Neg. uniaxial	660-9000
HgGa ₂ S ₄ (HGS)	Neg. Uniaxial	500-13000
LiGaS ₂ (LGS)	Biaxial	320-11600
LiGaSe ₂ (LGSe)	Biaxial	370-13200
LiInS ₂ (LIS)	Biaxial	400-11600
LiInSe ₂ (LISE)	Biaxial	500-12000

Table 3.1: List of mid-IR nonlinear crystals.

3.2 Requirements

In order for the crystals to be suitable for down-conversion of 1.55 μm and 2 μm radiation, a pre-requisite is that the transparency range must be able to accommodate both of these wavelengths and the down-converted pulse. For this we need the crystal to be transparent between approximately 1.4-9 μm . This leads us to discard ZGP and CGA. CSP has some absorption bands between 6.5 and 9 μm , but since short crystals will be used linear absorption should be a minor issue.

A second requirement before investigating the phase matching abilities is availability. AGS, AGSe, CS and GS are all commercial crystals that are easy to obtain and have been widely used for years. LIS, LISe, LGS, LGSe are not as well-known but extensive characterisation and fabrication improvement in recent years has led to a small number of companies distributing optical quality crystals of sufficient size for most nonlinear applications. CSP cannot be considered to be a commercial crystal, but also due to improvements in the growth process it is now possible to obtain optical quality parts from BAE systems. AAS, ASS, SPS, HGS, TAS and AGGS are not considered to be commercially available, even though some of these crystals are available in limited size and shapes from some institutions. Finally, it is decided that due its low nonlinearity and birefringence, CS is unsuitable for this system.

4 Evaluation of analytical solutions

As a first approximation the performance of the nonlinear crystals presented in Sec. 3 is estimated by numerically evaluating the analytical solutions for the DFG process derived in Sec. 2.2. These preliminary simulations are necessary to reduce the large parameter space before using the full 3D simulations, whose computational complexity makes scanning large parameter domains impractical. In particular in this section we find approximate values for the optimum propagation and noncollinear angles for each crystal based on phase matching considerations. This allows us to obtain a rough estimate of the phase matching bandwidth which we will use to evaluate the performance of the nonlinear crystals. The Sellmeier coefficients used to model the frequency dependent refractive index in following simulations can be found in Appendix A.

4.1 Analytical solutions

The expression to be numerically evaluated is an infinite plane wave solution of the coupled wave equations for the DFG process. The initial conditions that were used correspond to the physical situation in which the pump field is much stronger than the signal and can be considered constant throughout the nonlinear interaction. Typically, this expression is used to model OPA's:

$$I(\omega_i, l) = \frac{\omega_i}{\omega_s} I(\omega_s, l = 0) \cdot \sinh^2(lg), \quad (4.1)$$

where g is the parametric gain, given by:

$$g = \left(d_{eff}^2 \frac{2\omega_s \omega_i I(\omega_p)}{c^3 \epsilon_0 n(\omega_p) n(\omega_s) n(\omega_i)} - \left(\frac{\Delta k}{2} \right)^2 \right)^{1/2}. \quad (4.2)$$

It's arguable whether the actual physical case under consideration can be accurately modelled using Eq (4.1). In the first place, in our case the pump is only slightly stronger than the signal. This can be seen by comparing the peak intensities defined as $I_{peak} = E/(\tau A)$ where E is the energy contained in the pulse, τ is the temporal width measured at FWHM and A is the area of the beams. Assuming that the pump has $E = 2.5$ nJ, $\tau = 70$ fs and the signal has $E = 1.5$ nJ, $\tau = 130$ fs and that they both have the same beam size, the ratio of intensities between the two pulses is $I_p/I_s = (2.5 \cdot 100)/(1.5 \cdot 70) = 2.3$. This means that the assumption that the pump is much more intense than the signal is far from accurate. In second place, in the derivation of Eqn. 4.1 we assumed that the pump intensity was constant over the propagation distance. The validity of this assumption depends on many factors,

such as the value of d_{eff} or the length of the crystal. Nevertheless, the aim of this section is not to get an accurate physical description of the DFG process, but rather to obtain an estimate of the phase matching bandwidth and optimum propagation angles for each crystal. This is mainly controlled by the phase mismatch Δk , which is included in Eqn. 4.1 in the argument of the sinh. In spite of inaccuracies discussed above we expect that the numerical evaluation of the analytical solutions will give reasonably accurate values in terms of phase matching bandwidth and geometry.

For the purpose of comparing the behaviour of the different nonlinear crystals Eqn. 4.1 is evaluated in the following way: the pump is considered to be a monochromatic field at $1.5 \mu\text{m}$, while the signal is made up of discrete frequency components centred around $2 \mu\text{m}$. The idler frequencies are calculated by taking the difference between the pump frequency and the signal frequencies, $\omega_i = \omega_p - \omega_s$. Since the pump is monochromatic each idler frequency ω_i uniquely corresponds to a pair (ω_p, ω_s) which allows us to compute all the terms in Eqn. 4.1 and Eqn. 4.2 except for d_{eff} and l , which have to be introduced by hand.

The spectral width of the signal is chosen such that the idler spectrum spans 3500 nm of bandwidth. This is much larger than the bandwidth that will actually be attainable experimentally from the output of the Tm:Ho system (experimental consideration are discussed in the next section). The reason for taking such a large bandwidth is to obtain a broader picture of the phase matching abilities of the crystals beyond the restrictions of the particular laser system under consideration. This means of course that the phase matching bandwidths obtained in this section are only useful as a means of comparing the different crystals. On the other hand, the propagation and noncollinear angles computed with Eqn. 4.1 are expected to be accurate and are used in the next section as a starting point for the full 3D simulations.

4.2 Propagation directions and phase matching bandwidth

In the case of pulses presenting narrow spectra, the optimum propagation angle θ can be found with relative ease by minimising the phase mismatch function Δk for the central wavelengths of each input field. Since Δk is frequency dependant through the refractive indices, which generally vary little over small frequency ranges, phase matching the central wavelength is usually sufficient to obtain good phase matching for the rest of the spectrum. Finding an optimum noncollinear angle α is also simple in this case and can be found using the analytical expressions derived in Sec. 4.1. The situation is more involved when dealing with ultra-broadband pulses. The case at hand requires phase matching nearly 2000 nm of bandwidth. This leads to the question of how to choose optimum values for θ and α . For an ultra-broadband pulse, considering only the centre of gravity for phase matching is not enough since the effect of phase mismatch in other regions of the spectrum are neglected and can lead to unwanted reshaping of the idler spectrum and spectral narrowing. In

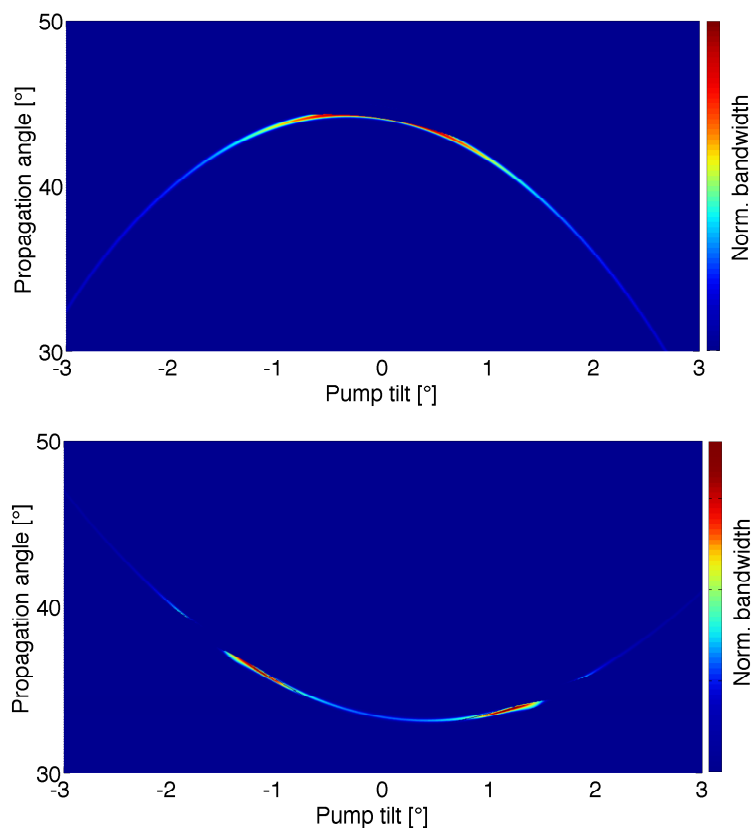


Figure 4.1: Noncollinear phase matching map for type I (o:o:e) interaction: (top) LIS, (bottom) AGS.

order to take into account the effect of phase mismatch on the whole spectrum, one possible approach is to compute $\Delta k(\omega, \theta, \alpha)$ and then integrate over ω for each pair of values (θ, α) . The minimum integral will give a first approximation to the optimum values for θ and α , although the actual dependence of the idler intensity with Δk is neglected in this case.

An improvement on this approach is achieved by directly computing $I(\omega_i, l)$ for each pair (θ, α) for an arbitrary value of l through numerical evaluation of Eqn. 4.1. The idler intensity curves with the largest spectral bandwidth will give an approximate set of phase matching values for θ and α . A useful way of showing this is plotting the idler bandwidth, which is arbitrarily taken at FWHM, as a function of α and θ . This gives a phase matching map for each crystal and phase matching type. As an example, the results for type I interaction in 5 mm of LIS and AGS are shown in Fig. 4.1 where we can see the curve described by the pairs of values (θ, α) that guarantee phase matching. For LIS, the simulations show that the broadest phase matching is obtained for propagation angles between 42° and 45° and non-collinear angles ranging between -1° and 1° . We can also see that for LIS, broadband phase matching is possible around $\alpha = 0$, while for AGS larger noncollinear angles are needed. In this case broadband phase matching is obtained in two separate regions of the map.

By taking the width of the broadest idler phase-matchable $I(\omega_i, l)$ we can assign a value to the phase matching bandwidth of each crystal. The approximate phase matching angles and corresponding idler bandwidth for collinear and noncollinear geometries are summarised in Tab. 4.1. It's worth noting that an arbitrary propagation length of 5 mm was used for these simulations. The actual interaction length of the pulses will be shorter than this in most cases due to temporal and spatial walkoff.

The results show that the phase matching bandwidth is considerably improved using noncollinear geometry for nearly all the crystals. The only exception is LIS in type I (o:o:e) interaction due to the fact that the optimum noncollinear angle is close to zero, as can be seen in the phase matching map shown in Fig. 4.1. Based on the phase matching bandwidth of the crystals, the results allow us to discard a number of candidates for the DFG. This is the case of AGSe type I (o:o:e) and CSP type II (e:o:e). In addition, GS type I (o:o:e) and GS type II (e:o:e) are also discarded for technical reasons: as discussed in Sec. 3 the crystal can only be cut in the (001) plane (perpendicular to the optical axis) which means that only parts with $\theta = 0^\circ$ are available. Even though the phase matching angles are small, the refractive index of GS is high and the corresponding external signal angles, over 45° for a 13° internal angle, are big enough to lead to severe angular chirp that in a broadband pulse as well as increased Fresnel losses.

Crystal	PM type	θ_c [°]	BdW _c [μm]	θ_{nc} [°]	α [°]	BdW _{nc} 1 [μm]
AGSe	I (o:o:e)	68.0	<0.5	85.0	1.8	0.5
AGS	I (o:o:e)	34.0	<0.5	35.0	1.5	2
AGS	II (e:o:e)	40.0	<0.5	53.5	2.9	1
CSP	I (o:o:e)	54.5	<0.5	63.5	1.8	1.5
CSP	II (e:o:e)	71.5	<0.5	80.0	1.0	0.5
GS	I (o:o:e)	13.5	<0.5	13.0	2.2	1.5
GS	II (e:o:e)	15.5	<0.5	21.0	3.4	1
LGS	I (o:o:e) (XZ)	48.5	1.0	47.5	0.8	2
LGS	II (e:o:e) (XY)	44.3	0.5	49.5	1.8	1.5
LGSe	I (o:o:e) (XZ)	55.0	0.5	50.5	1.5	2
LGSe	II (e:o:e) (XY)	35.0	<0.5	44.0	2.4	1.5
LIS	I (o:o:e) (XZ)	44.0	2.5	43.5	0.5	2.5
LIS	II (e:o:e) (XY)	35.0	<0.5	47.0	2.4	1.5
LISe	I (o:o:e) (XZ)	43.5	0.5	35.5	1.9	1
LISe	II (e:o:e) (XY)	34.5	<0.5	56.5	3.5	1

Table 4.1: Phase matching angles and computed idler bandwidth for collinear and noncollinear interaction after 5 mm of propagation. The propagation plane is included for the biaxial crystals. PM is the phase matching type, θ_c and BdW_c are the phase matching angle and bandwidth of the idler in collinear interaction, θ_{nc} is the signal propagation angle in noncollinear interaction, α is the noncollinear angle and BdW_{nc} is the bandwidth of the idler in noncollinear interaction

5 Simulations of DFG as an OPCPA seed

The parameter space involved in choosing the non-linear crystal and setup design for this system is large and many of the parameters that need to be scanned are coupled to one another. A number of geometrical setups, established namely through the propagation angle, noncollinear angle and crystal length need to be investigated for each crystal. In addition, the values of the second order susceptibility tensor and the phase mismatch, which are the quantities that drive the process, depend on these geometrical arrangements which in turn will influence the temporal and spatial evolution of the pulses during the amplification process. Thus a thorough understanding of the DFG process itself is needed that cannot be obtained through use of numerical evaluation of simple analytical solutions. Many of the codes used to model nonlinear processes are one or two dimensional and neglect interactions that limit spatial and temporal overlap of the pulses, while experimentally these effects are crucial.

In this work the 3D nonlinear propagation code Sisyfos based on the numerical model described in Sec. 2.3 is used. The nonlinear propagation equations are solved in the Fourier domain using a Runge-Kutta algorithm. This code was developed at Forsvarets ForskningsInstitutt (FFI) and has already proved its ability to model nonlinear interactions accurately [47, 48]. It accounts for most of the physical phenomena involved in the process, such as dispersion, birefringence, quantum noise, non-collinear interaction, linear absorption, thermal effects, temporal and spatial walkoff and beam distortion. The limitations of the analytical model shown in Sec. 2.2 are obvious in comparison. However, it is important to keep in mind that a numerical model is never completely accurate. This can be attributed to either the theoretical approximations in the model or to the inaccuracy of the parameters and constants involved in the computation. Apart from the approximations used in this code, which were discussed in Sec. 2.3, many of the physical quantities that determine the efficiency and characteristics of the process, such as the values of the second order susceptibility tensor or the frequency dependent refractive index, are rarely known with precision and can vary from crystal to crystal. The same is true for the characteristics of the input pulses. Therefore, the simulation results should be taken as a guideline rather than as an absolute prediction of what to expect from the experimental setup.

Apart from the choice of nonlinear crystal, the goal of these simulations is to find the optimum design parameters for the DFG stage. The main simulation parameters corresponding to physical variables can be separated into two groups. The first are those parameters related to the characteristics of the input pulses, which are mainly determined by the output of the Tm:Ho system. The spectrum and energy of the signal and pump pulses have fixed values

that can be measured directly. In principle the pulse duration can be set at an arbitrary value within the limits set by the bandwidth since the pulses can be stretched and compressed, but in this case we are interested in obtaining the highest possible peak power, which is given for the shortest pulses. This is also the case for the beam size, which is only limited by the focusability of the beams. The second group of parameters are the free parameters that will determine the design of the DFG stage: crystal length, propagation direction (given by the angle between the signal and the optical axis), non-collinear angle (taken as the angle between the signal and the pump) and phase-matching type. These variables are explored through use of the numerical simulations in order to find the optimum setup configuration.

This section is organised as follows. First the experimental issues related to the input parameters and the targeted output for the DFG simulations are briefly discussed. Then the full 3D simulations performed with Sisyfos are used to study the DFG process in LGS, LGSe, LIS, LISe, CSP, and AGS. The optimum propagation and noncollinear angles are found and used to find the output idler pulse energy and bandwidth as well as study the underlying physical processes involved. Finally, the simulation results are used to compare the performance of the different crystals.

5.1 Input parameters for the simulations

Next we discuss the input parameters used to model the pump and signal beams based on the experimental data obtained from the Tm:Ho system. The spectrum of the 1.55 μm broadband pump and the 2 μm broadband signal are shown in Fig. 5.1. The spectra span 1.50 to 1.64 μm and 1.99 to 2.07 μm at $1/e^2$. The average power at the output of the Tm:Ho is 350 mW and 320 mW for the pump and signal respectively, which at the repetition rate of 100 MHz yields pulse energies of 3.5 nJ and 3.2 nJ. The 1.5 μm output is internally compressed to a pulse duration of 70 fs while the 2 μm is uncompressed and reveals a pulse duration in the ps range. In the actual experimental setup, the pump is expected to suffer a minimum amount of losses, mostly due to reflection off metallic mirrors. The signal on the other hand will need to be compressed, which is an intrinsically lossy process. Taking these losses into account the average power expected to be available for the DFG process is approximately 250 mW and 150 mW for the pump and signal beams respectively.

Taking into account the experimental data presented above, the input pulses are modelled as follows. For simplicity, the pump and signal spectra are defined using a gaussian profile centred at 1.55 μm and 2.03 μm with a bandwidth of 90 and 65 nm at FWHM respectively. The pulse duration is set to 70 and 100 fs by applying a negative linear chirp to the pulses. The pump energy is set to 2.5 nJ while the signal is set to 1.5 nJ. Finally, the beam diameter is set to 20 μm radius at FWHM. This leads to peak intensities of 3 GW/cm^2 for the pump and 1.3 GW/cm^2 for the signal.

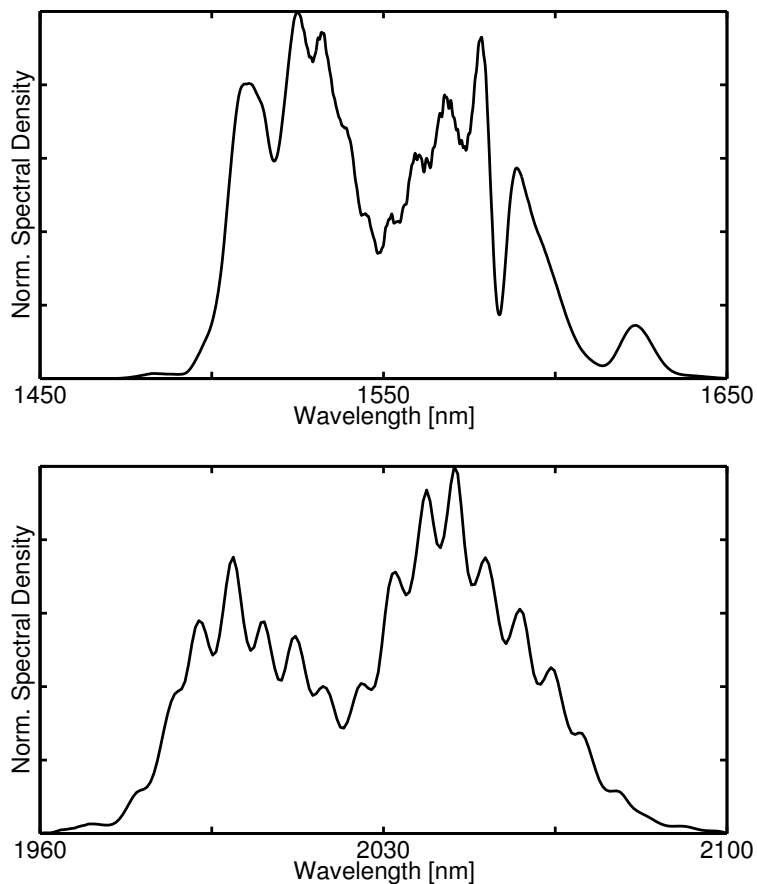


Figure 5.1: Measured spectrum of the input pulses for the DFG: (top) 1.55 μm broadband pulse and (bottom) 2.03 μm broadband signal.

5.2 Target output parameters

The output parameters that are most relevant when comparing the nonlinear crystals are essentially the spectral bandwidth and energy of the output idler pulse. The other parameters involved in the process, such as spatial and temporal walkoff, dispersion, etc. are less useful for direct comparison. They can however be used to improve the design of each specific setup. As an example, it is common practice to improve the efficiency of a crystal with a large spatial walkoff by tilting the extraordinary beam to compensate for the walkoff and thus increase the interaction length. A similar approach can be followed in the temporal domain to mitigate temporal walkoff effects by delaying the input pulses with respect to one another such that the slower pulse enters the crystal before the faster pulse.

One way of establishing a target idler bandwidth is calculating the optimum output of the DFG stage. This can be done by convoluting the pump and signal spectra, which is physically equivalent to mixing two unchirped input pulses in a crystal with no phase mismatch and gives a best-case scenario in terms of bandwidth. The result, shown in Fig. 5.2, shows that the maximum bandwidth attainable with the input pulses is roughly 1750 nm at

the centre of gravity of $7.1 \mu\text{m}$. This bandwidth gives a transform limited pulse with less than 2 optical cycles.

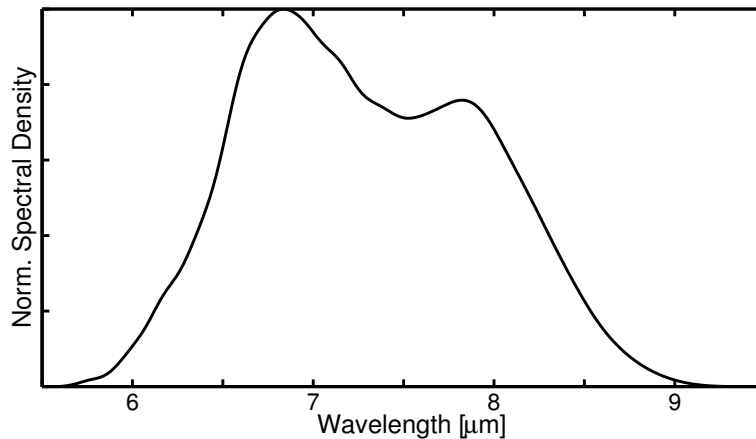


Figure 5.2: Computed optimum DFG output spectra

The target output pulse energy is not as straightforward to establish. This is due to the fact that the spectral bandwidth and conversion efficiency are coupled. If we ignore spatial and temporal walk-off and pump and signal depletion, the idler pulse energy grows monotonically with propagation distance. But due to the dependence of the phase mismatch with propagation distance, in general a longer interaction length will lead to spectral narrowing. This means that a balance has to be found between bandwidth and output energy. Thinking in broader terms, the subsequent amplification stages in the OPCPA system can compensate for low seed power while gaining bandwidth requires complicated and costly techniques. Therefore the bandwidth of the output idler pulse is taken as the main parameter to be taken be optimised while comparing the performance of the different nonlinear crystals.

5.3 Numerical simulation results

It was shown in Sec. 4 that the crystals that remain as suitable candidates for the DFG stage due to their phase matching bandwidth are LGS, LGSe, LIS, LISe, CSP and AGS. Apart from the approximations used to derive the analytical expressions, some discrepancies in terms of phase matching configurations are to be expected between the full 3D simulations with Sisyfos and numerical evaluation of the analytical solutions of the previous section. This is mainly due to differences in the spectra used to model the pulses. Therefore as a first step, low resolution simulations are carried out to check the validity of the results from the previous section in terms of phase matching angles and estimated bandwidth. These preliminary simulations with Sisyfos confirm that AGSe type I (o:o:e) and CSP type II (e:o:e) are unsuitable for the DFG stage due to their narrow output idler spectra. They also show that LISe in both type I (o:o:e) and type II (e:o:e) interaction presents narrow phase matching

even for noncollinear geometry. Consequently, CSP type II, AGSe type I and LISe type I and II are discarded and are not included in the following.

The Sellmeier coefficients used to model the frequency dependent refractive index in following simulations can be found in Appendix A. The values for the nonlinear coefficient d_{eff} are taken from the program SNLO developed by Dr. Arlee Smith at Sandia National Laboratories. A summary of the simulation results can be found at the end of this section in Tab. 5.2 and Tab. 5.3.

5.3.1 LGS

Of all the nonlinear crystals considered, LGS has the lowest nonlinear coefficient. In particular for type I phase matching in the XZ plane, the value of d_{eff} is 3.9 pm/V. On the other hand the damage threshold is higher than for any of the other crystals considered in this section, over an order of magnitude higher than AGS or CSP, allowing higher peak powers that can help compensate for the low interaction strength. The simulations show that the crystal is not suitable for type I (o:o:e) interaction in either collinear or noncollinear geometry, for which the optimum values of $\theta_c = 47.8^\circ$ and $\theta_{nc} = 47.2^\circ, \alpha = 0.4^\circ$ were found. After 3 mm of propagation the idler pulse energy obtained at the output is less than 20 pJ in both cases. Figure 5.3 shows the evolution of the idler pulse energy and bandwidth throughout the crystal. The main cause for the low efficiency is a combination of a small d_{eff} and non-optimal phase matching even at the optimum phase matching angles. Temporal and spatial walkoff effects are not severe in this case, which means that a longer crystal will result in a slight improvement.

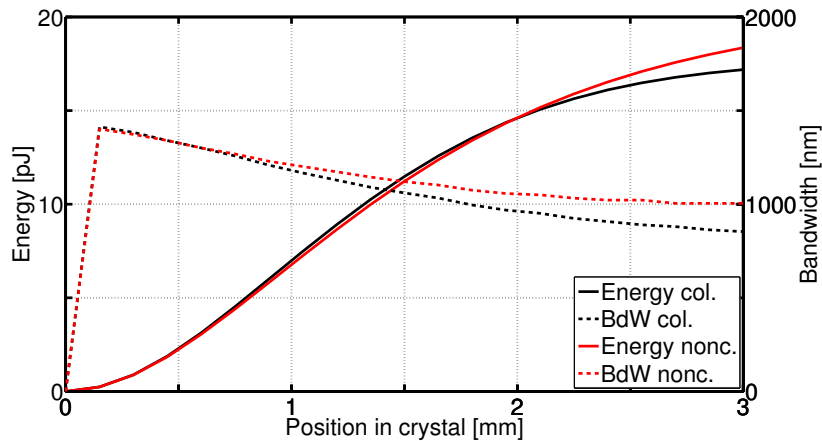


Figure 5.3: Evolution of the idler pulse energy (straight line) and bandwidth at FWHM (dotted line) as a function of propagation distance for type I phase matching in an LGS crystal. The black and red line correspond to collinear and noncollinear geometry respectively.

The performance of the crystal is improved by use of type II (e:o:e) interaction where broadband phase matching is possible using collinear geometry as is shown in Fig. 5.4. This

is mainly due to a higher nonlinearity, $d_{eff} = 5.7$ pm/V in this case, although the value is still comparatively small. The optimum geometry in this case was found to be $\theta_c = 42^\circ$ and $\theta_{nc} = 52.5^\circ, \alpha = 1.9^\circ$. Using collinear geometry we obtain idler pulses of 40 pJ and a bandwidth of over 1200 nm for a 3 mm crystal. The temporal walkoff is worse than for type I interaction and increasing the interaction length in this case leads to little improvement in the idler pulse energy. At the output of the crystal the temporal overlap of the pulses is small since the pump and signal are delayed by 80 fs. The idler bandwidth can be further improved through use of noncollinear geometry but an increase in temporal walkoff causes the interaction length to shorten even further. Nevertheless we obtain 1500 nm of bandwidth and idler pulse energies of 35 pJ after 3 mm of propagation, which is among the largest bandwidths found among any of the nonlinear crystals.

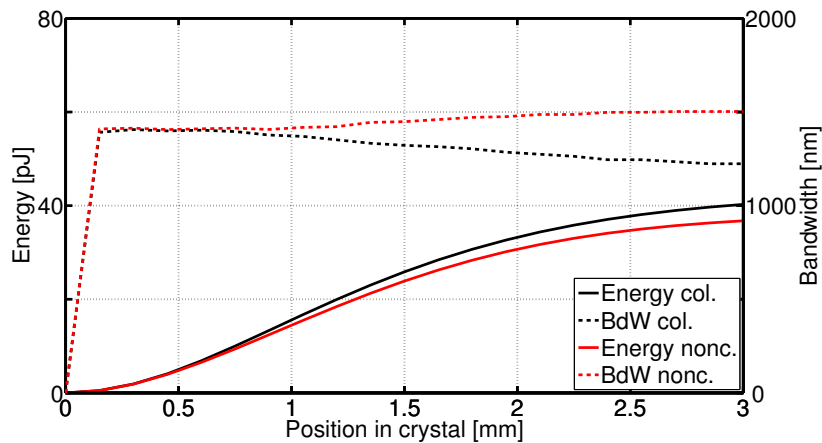


Figure 5.4: Evolution of the idler pulse energy (straight line) and bandwidth at FWHM (dotted line) as a function of propagation distance for type II phase matching in an LGS crystal. The black and red line correspond to collinear and noncollinear geometry respectively.

An interesting behaviour that can be observed for noncollinear geometry in Fig. 5.4 is the fact that the idler bandwidth slightly increases with propagation distance over the first 2 mm. This is the opposite of what is expected from the analytical solutions discussed previously, which predict that the phase mismatch increases with propagation distance effectively suppressing the nonlinear interaction. The reason behind this is the temporal dependence of the phase in the input pulses combined with the group velocity mismatch (GVM). For zero GVM the pump and signal pulses travel together over the crystal and the front and back ends of the pulses are always overlapped. If the pulses are chirped, this means that less idler frequencies are being generated since less pump and signal frequencies are being mixed. This effect is always present but is only noticeable when the phase matching is broadband enough.

The nonlinear code used here offers the unique possibility of studying the effect of noncollinear geometry on the output spatial intensity profile of the idler beam in 3D. This is of vital importance since beam distortion can limit the practical feasibility of a noncollinear

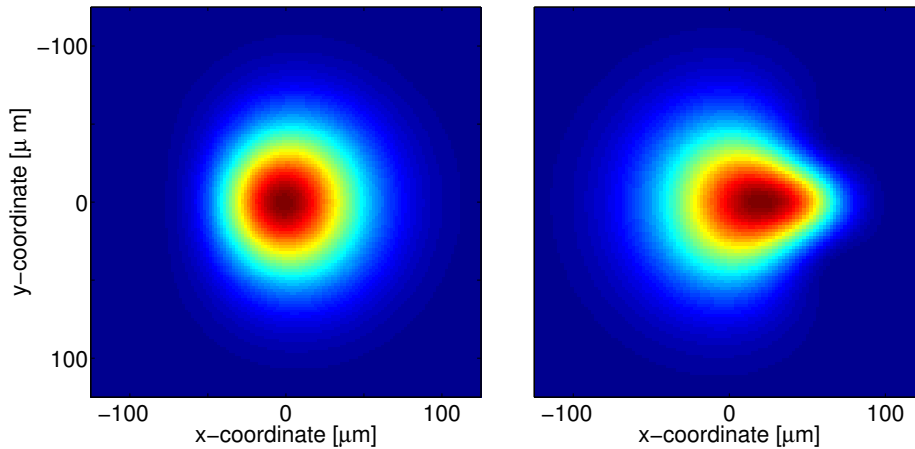


Figure 5.5: Idler beam profile after propagating 3 mm in noncollinear geometry in LGS for type I interaction with $\alpha = 0.4^\circ$ (left) and type II interaction with $\alpha = 1.9^\circ$ (right). The scale used for the two plots is the same to facilitate comparison of distortion effects.

setup, which can be overlooked when accounting for phase matching and temporal and spatial overlap alone. Fig. 5.5 shows the idler beam profile for type I and type II interaction after 3 mm of propagation in LGS. For type I phase matching the small noncollinear angle leads to a negligible beam asymmetry. For type II phase matching the noncollinear angle is nearly five times larger and the beam profile is visibly distorted. In this case the beam profile is made worse in type II interaction due to the additional spatial walkoff effect on the idler.

5.3.2 LGSe

LGSe has the same structure and symmetry as LGS but slightly higher nonlinearity, for type I (o:o:e) interaction $d_{eff} = 6.1$ pm/V. In collinear geometry, we obtain idler pulse energies of around 30 pJ and a bandwidth of 1050 nm after 3 mm of propagation and a propagation angle of $\theta = 55.5^\circ$. The evolution of the idler pulse is shown in Fig. 5.15. The idler pulse energy saturates completely before the end of the crystal due to spatial walkoff of the pump, which means that in this case using a shorter crystal will increase the bandwidth without decreasing the output energy. Use of noncollinear geometry with $\theta_{nc} = 51.4^\circ$, $\alpha = 1.4^\circ$ yields an increase of 500 nm in bandwidth accompanied by a modest increase in efficiency. However, there is a notable reduction in spatial and temporal walkoff as well as a constant bandwidth evolution which would allow us to use, at least in principle, a longer crystal to increase the interaction length. The downside of this of course is beam distortion due to the noncollinear angle, which will tend to get worse with propagation distance. Fig. 5.8 shows the idler beam distortion after 3 mm of propagation.

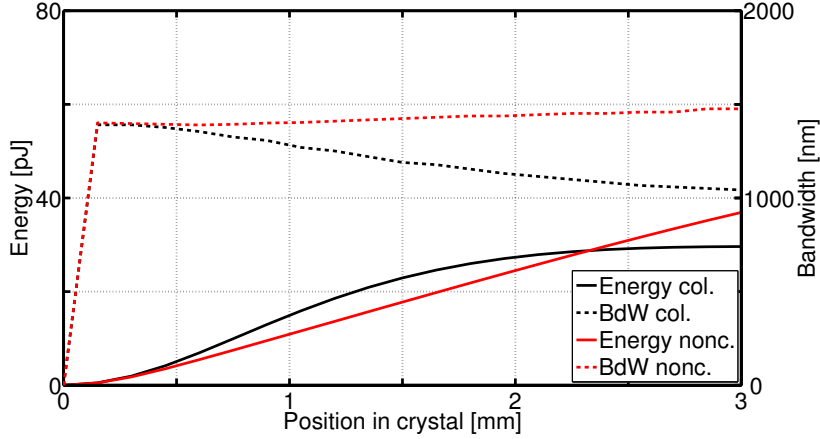


Figure 5.6: Evolution of the idler pulse energy (straight line) and bandwidth at FWHM (dotted line) as a function of propagation distance for type I phase matching in an LGSe crystal. The black and red line correspond to collinear and noncollinear geometry respectively.

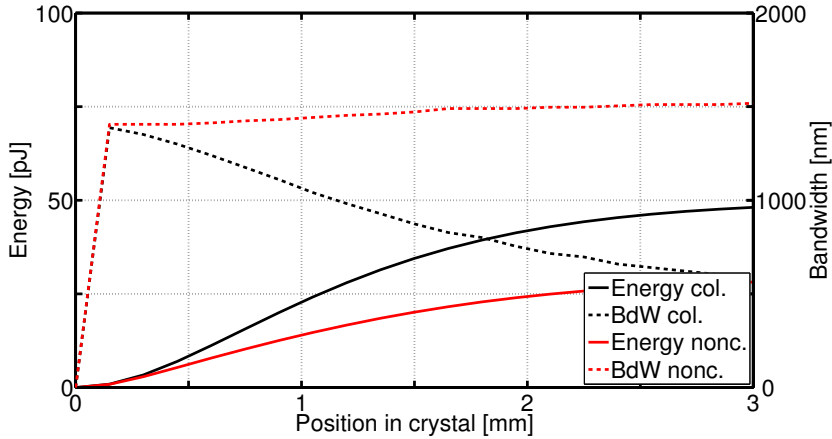


Figure 5.7: Evolution of the idler pulse energy (straight line) and bandwidth at FWHM (dotted line) as a function of propagation distance for type II phase matching in an LGSe crystal. The black and red line correspond to collinear and noncollinear geometry respectively.

LGSe presents a relatively large nonlinearity for type II (e:o:e) interaction, $d_{eff} = 8.7$ pm/V, the largest value for any of the Lithium-based chalcogenides. The optimum angles in this case are $\theta_c = 33.5^\circ$ and $\theta_{nc} = 43.5^\circ$, $\alpha = 2.2^\circ$. The simulations show that the GVM between the pump and signal is low: after 3 mm of propagation the delay between the input pulses is around 10 fs for the collinear case, thus ensuring that the pulses are completely temporally overlapped throughout the crystal. The spatial walkoff causes the idler pulse energy to reach a maximum value after approximately 3 mm of propagation. Unfortunately the phase matching bandwidth is narrow, as shown in Fig. 5.7. For a 3 mm crystal we obtain less than 600 nm of bandwidth and a pulse energy of 50 pJ. The phase matching can be greatly improved using noncollinear geometry, see Fig. 5.7, although at the cost of

losing half of the output energy due to an increase in the temporal walkoff and a decreased interaction length. Also the noncollinear angle needed to obtain broadband phase matching is large, leading to the severe beam distortion shown in Fig. 5.8.

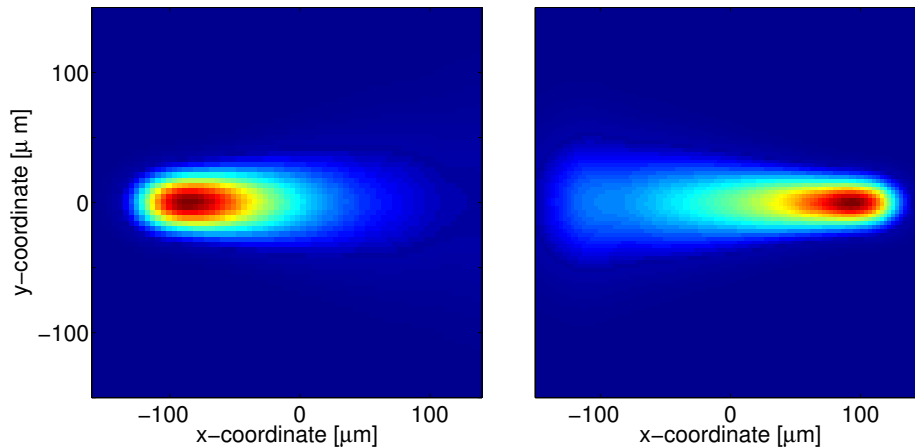


Figure 5.8: Idler beam profile after propagating 3 mm in noncollinear geometry in LGSe for type I interaction with $\alpha = 1.4^\circ$ (left) and type II interaction with $\alpha = 2.2^\circ$ (right). The scale used for the two plots is the same to facilitate comparison of distortion effects.

5.3.3 LIS

LIS has the interesting ability of being able to sustain broadband phase matching using collinear geometry. This has the advantage of simplifying the experimental setup as well as improving the beam quality. In the case of type I (o:o:e) interaction, which presents a low nonlinearity with $d_{eff} = 5.3$ pm/V and for which an optimum angle of $\theta_c = 44^\circ$ was found, idler pulses with 1200 nm of bandwidth and 40 pJ were obtained. This is the same output as the one obtained for LGS in type II collinear interaction. The simulations show that the performance can be optimised by tilting the pump by an angle of $\alpha = 0.6^\circ$ and setting $\theta_{nc} = 44.3^\circ$. This leads to an increase in 200 nm of bandwidth. The efficiency is also slightly improved due to compensation of the pump spatial walkoff and 50 pJ of idler pulse energy are obtained. Additionally, as can be seen in Fig. 5.9, the energy of the idler shows no sign of reaching its maximum after 3 mm of propagation which together with the constant bandwidth evolution means that using a longer crystal is feasible. Although such a small angle leads to an excellent beam profile, see Fig. 5.11, it also leads to experimental issues. The external angle between the signal and pump needed in this case is around 1.3° , which is difficult to achieve in a setup where very tight focusing is required.

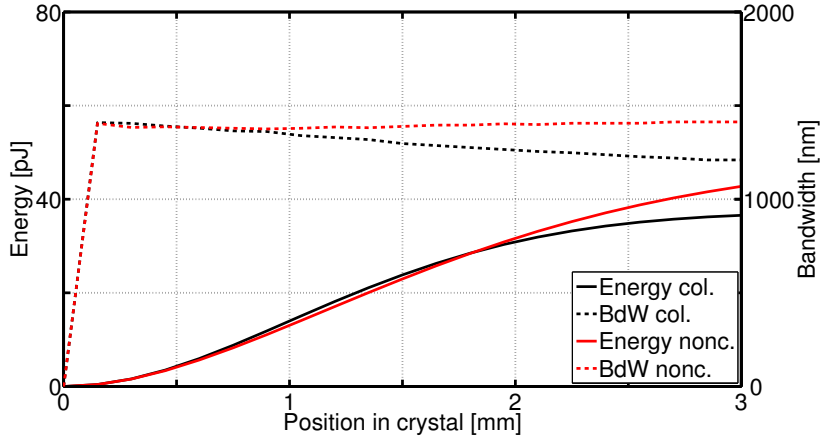


Figure 5.9: Evolution of the idler pulse energy (straight line) and bandwidth at FWHM (dotted line) as a function of propagation distance for type I phase matching in an LIS crystal. The black and red line correspond to collinear and noncollinear geometry respectively.

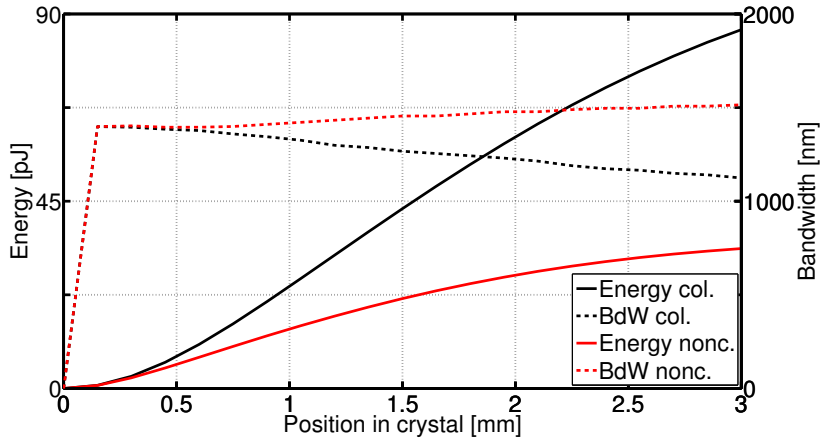


Figure 5.10: Evolution of the idler pulse energy (straight line) and bandwidth at FWHM (dotted line) as a function of propagation distance for type II phase matching in an LIS crystal. The black and red line correspond to collinear and noncollinear geometry respectively.

LIS shows a higher nonlinearity for type II interaction, where $d_{eff} = 7.2$ pm/V. Together with good phase matching, obtained for $\theta_c = 34^\circ$ and small spatial and temporal walkoff this leads to idler pulses with energies of up to 90 pJ and over 1100 nm of bandwidth after 3 mm of propagation, see Fig. 5.10. Even though the spectrum is narrower than in the type I case, the conversion efficiency is so much higher that a shorter crystal can be used to obtain the same bandwidth with higher pulse energy. For instance, a crystal of 1.5 mm would give 1250 nm of bandwidth with idler pulse energies of around 45 pJ. Tilting the pump by $\alpha = 1.7^\circ$ and setting $\theta_{nc} = 43^\circ$ leads to an increase of nearly 400 nm in bandwidth, but also to a large drop in efficiency caused by temporal walkoff. Additionally as opposed to the type I case, the optimum noncollinear angle is large, leading to the severe beam distortion that is shown in Fig. 5.11.

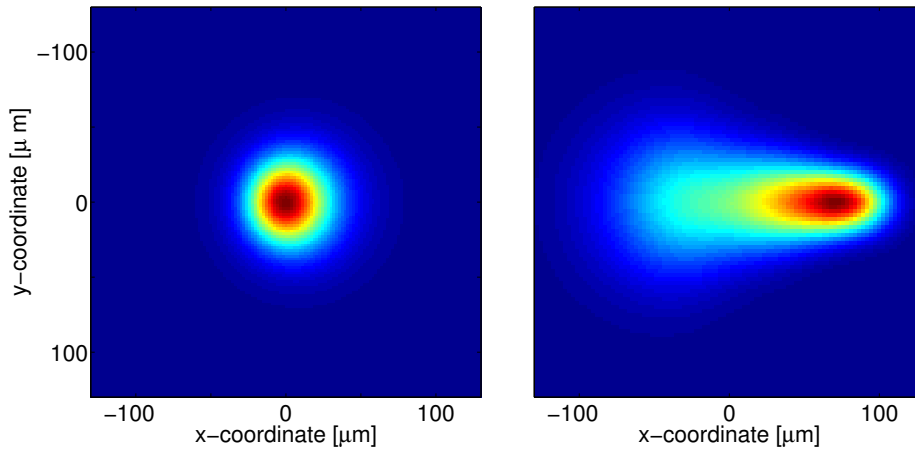


Figure 5.11: Idler beam profile after propagating 3 mm in noncollinear geometry in LIS for type I interaction with $\alpha = 0.6^\circ$ (left) and type II interaction with $\alpha = 1.7^\circ$ (right). The scale used for the two plots is the same to facilitate comparison of distortion effects.

5.3.4 CSP

CSP has by far the largest nonlinearity of all the crystals considered in this work, for type I (o:o:e) interaction $d_{eff} = 43$ pm/V. This leads to complicated dynamics introduced by pump depletion and back-conversion effects which are not observed in any of the other crystals due to their comparatively low conversion efficiency. Understanding the physical processes involved and choosing an optimum configuration is therefore more challenging than in the other cases and the energy evolution of the signal and pump must be taken into account. Figure 5.12 shows the evolution of the idler bandwidth and pulse energy. For collinear geometry using $\theta_c = 51.9^\circ$ the pulse energy of the idler reaches its maximum value at 145 pJ after around 1 mm of propagation. As opposed to the other crystals, where the energy conversion is reduced by temporal and/or spatial walkoff effects, in this case back-conversion is reached and idler energy is being transferred back to the pump and signal. This leads to the pump spectrum being distorted which in turn causes the idlers spectrum to reshape. After 3 mm of propagation we obtain pulses of 120 pJ and 1000 nm of bandwidth. Increasing the propagation length is not beneficial in this case due to temporal walkoff.

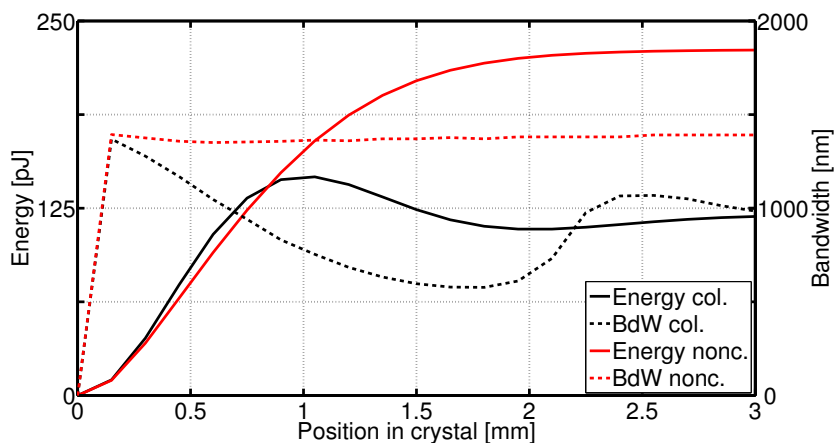


Figure 5.12: Evolution of the idler pulse energy (straight line) and bandwidth at FWHM (dotted line) as a function of propagation distance for type I phase matching in a CSP crystal. The black and red line correspond to collinear and noncollinear geometry respectively.

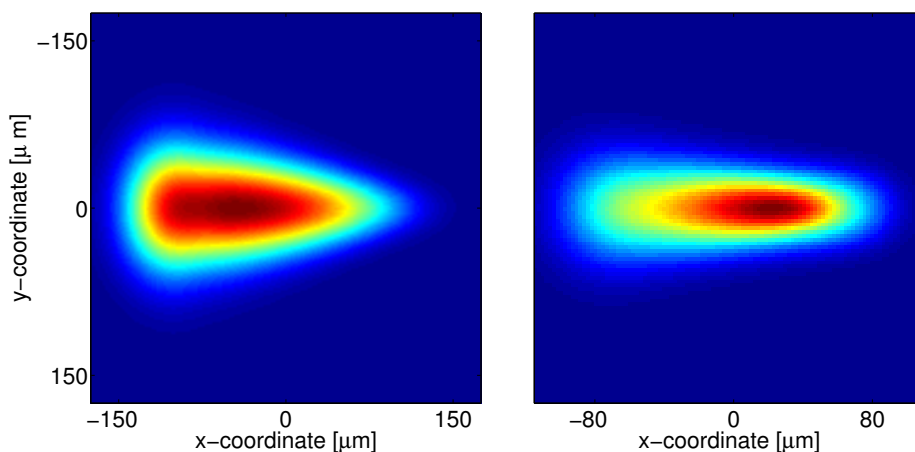


Figure 5.13: Idler beam profile for type I noncollinear interaction in CSP with $\alpha = 1.9^\circ$ after propagating 3 mm (left) and 1.5 mm (right). Note that the scale is not the same for the two plots.

A dramatic increase in both bandwidth and energy can be obtained through use of noncollinear geometry with $\theta_{nc} = 66.7^\circ$ and $\alpha = 1.9^\circ$. Back-conversion is avoided in this case and the energy of the idler grows monotonically until saturating after 2 mm of propagation at 230 pJ due to spatial walkoff. Phase matching is also improved and the bandwidth shows a constant evolution at 1400 nm. The temporal walkoff in CSP case is large for both collinear and noncollinear geometries. In the noncollinear case after 3 mm the pump and signal are delayed by 120 fs. This means that the efficiency of the process can be improved even further by fine tuning the temporal delay between the input pulses, which is something that can be easily implemented experimentally. However, the noncollinear angle needed to obtain

broadband phase matching is large enough that the idler beam profile is heavily distorted. Figure 5.13 show the idler beam profile after 3 mm and 1.5 mm of propagation.

5.3.5 AGS

In the case of collinear type I (o:o:e) interaction, which presents a nonlinearity of $d_{eff} = 7.5$ pm/V and for an optimum angle of $\theta_c = 34^\circ$, idler pulses with 900 nm of bandwidth and 30 pJ were obtained. Both the temporal and spatial walkoff effects are large enough that the idler pulse energy reaches its maximum value after less than 2 mm of propagation. By use of noncollinear geometry with $\theta_{nc} = 37.5^\circ, \alpha = 1.6^\circ$ the bandwidth can be increased to 1400 nm and the idler plus energy to 35 pJ.

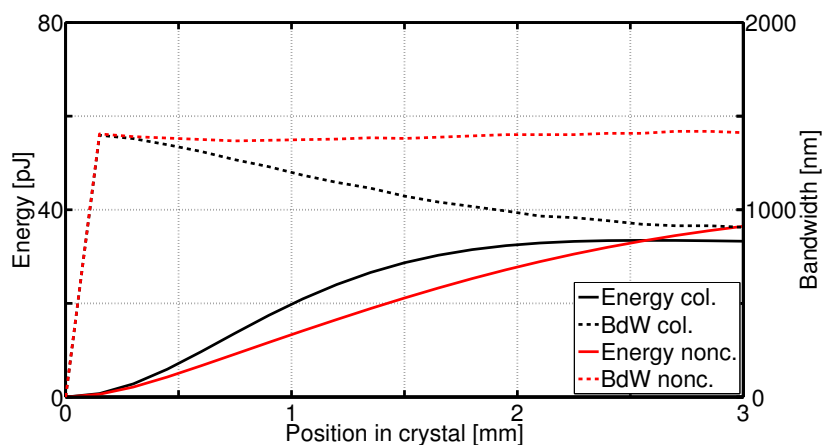


Figure 5.14: Evolution of the idler pulse energy (straight line) and bandwidth at FWHM (dotted line) as a function of propagation distance for type I phase matching in an AGS crystal. The black and red line correspond to collinear and noncollinear geometry respectively.

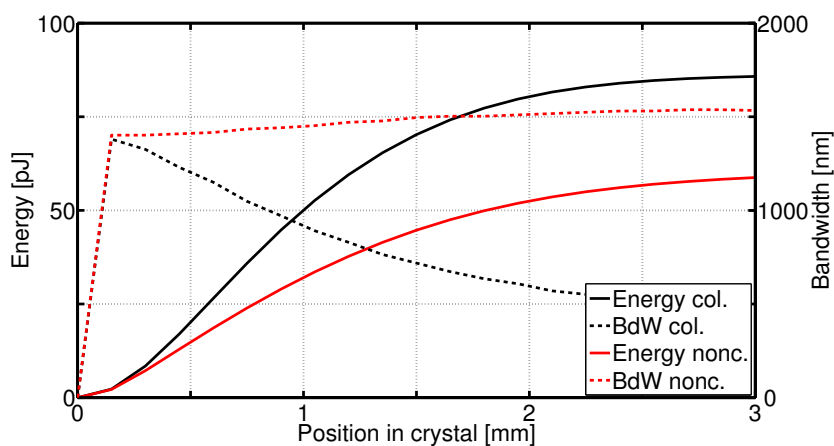


Figure 5.15: Evolution of the idler pulse energy (straight line) and bandwidth at FWHM (dotted line) as a function of propagation distance for type II phase matching in an AGS crystal. The black and red line correspond to collinear and noncollinear geometry respectively.

The nonlinearity of AGS is considerably higher in type II interaction, $d_{eff} = 15$ pm/V compared to $d_{eff} = 7.5$ pm/V for type I. Also the severe temporal walkoff limiting the interaction length in the type I collinear case is improved leading to a high conversion efficiency. Using the optimum propagation angle $\theta_c = 40.5^\circ$, after 3 mm of propagation idler pulses of 85 pJ are obtained, but due to narrow phase matching the bandwidth was less than 500 nm. A large noncollinear angle is needed to obtain broadband phase matching, the optimum angles were found to be $\theta_{nc} = 52^\circ$ and $\alpha = 2.5^\circ$. The resulting shortening of the interaction length limits the conversion efficiency and leads to a reduction in output energy down to 55 pJ with a bandwidth of over 1500 nm. The beam distortion is quite severe and can be seen in Fig. 5.16.

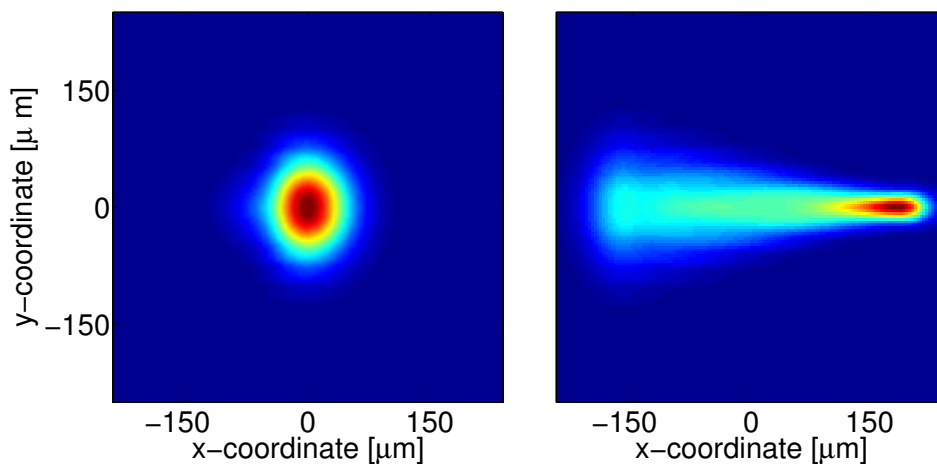


Figure 5.16: Idler beam profile after propagating 3 mm in noncollinear geometry in AGS for type I interaction with $\alpha = 1.3^\circ$ (left) and type II interaction with $\alpha = 2.5^\circ$ (right). The scale used for the two plots is the same to facilitate comparison of distortion effects.

5.4 Optimum crystal and configuration

Using the results obtained for the DFG stage from the simulations with Sisyfos we are now in a position to choose an optimum configuration for each crystal. The type of interaction, propagation angles and resulting idler bandwidth and energy are shown in Tab. 5.1. Clearly CSP outperforms the rest of the crystals in terms of energy, which was to be expected given the huge difference between the values of d_{eff} . The crystal length is chosen to be 1.5 mm as a compromise between energy conversion and beam distortion. Although LIS cannot compete with CSP in energy conversion, it can be used for broadband phase matching with a small noncollinear angle, leading to a symmetric beam profile with no distortions. AGS shows the broadest phase matching of any of the crystals, but the large noncollinear angle leads to dramatic beam distortions, which is why in this case the propagation length is also

shortened. Finally, LGS and LGSe are outperformed by LIS in terms of beam quality and energy while the difference in bandwidth is less than 10%.

Crystal	PM type	θ [°]	α [°]	Length [mm]	BdW 1[μm]	Energy [pJ]
LGS	II (o:o:e) (XY)	44.8	1.9	3	1500	35
LGSe	I (o:o:e) (XZ)	51.4	1.4	3	1500	35
LIS	I (o:o:e) (XZ)	43.1	0.6	3	1400	50
CSP	I (o:o:e)	66.7	1.9	1.5	1400	200
AGS	II (e:o:e)	00.0	2.5	2	1550	50

Table 5.1: Optimum configuration for each crystal and computed output.

The simulation results strongly suggest that CSP is the optimum crystal for the DFG stage being designed. The small difference in bandwidth with respect to the other crystal is made up for in pulse energy, since the gain requirements on the subsequent OPA stages are relaxed and spectral gain narrowing will be less severe.

5.5 Summary of results

	LIS Type I	LIS Type II	LGSe Type I	LSGe Type II	LGS Type I	LGS Type II	CSP Type I	AGS Type I	AGS Type II
$E(z=1)$ [pJ]	15	25	15	25	5	15	145	20	50
$E(z=2)$ [pJ]	30	60	25	40	15	35	111	30	80
$E(z=3)$ [pJ]	35	85	30	50	15	40	120	35	85
$BdW(z=1)$ [nm]	1350	1325	1275	1075	1175	1375	975	1200	900
$BdW(z=2)$ [nm]	1375	1225	1125	750	950	1275	625	975	600
$BdW(z=3)$ [nm]	1200	1125	1050	575	850	1225	750	900	475
$W_{temp}(z=3)$ [fs]	35	25	50	10	30	80	150	85	30
$W_{spat}(z=3)m$ [μ m]	60	50	65	65	60	55	35	60	65

Table 5.2: Simulation results for a collinear DFG stage. $E(z)$ is the idler pulse energy, $BdW(z)$ is the bandwidth of the idler measured at FWHM, $W_{temp}(z)$ is the temporal walkoff between the pump and signal, $W_{spat}(z)$ is the spatial walkoff between the pump and signal, and z is the propagation distance measured in mm.

	LIS Type I	LIS Type II	LGSe Type I	LSGe Type II	LGS Type I	LGS Type II	CSP Type I	AGS Type I	AGS Type II
$E(z=1)$ [pJ]	15	15	10	15	5	15	160	15	30
$E(z=2)$ [pJ]	30	25	25	25	15	30	225	30	50
$E(z=3)$ [pJ]	50	35	35	30	20	35	225	35	55
$BdW(z=1)$ [nm]	1375	1425	1400	1450	1200	1400	1350	1400	1450
$BdW(z=2)$ [nm]	1400	1475	1450	1500	1050	1475	1375	1425	1500
$BdW(z=1)$ [nm]	1400	1515	1475	1525	100	1500	1400	1425	1525
$W_{temp}(z=3)$ [fs]	25	60	25	50	35	90	120	90	40
$W_{spat}(z=3)m$ [μ m]	30	35	5	50	65	5	80	130	65

Table 5.3: Simulation results for a noncollinear DFG stage. $E(z)$ is the idler pulse energy, $BdW(z)$ is the bandwidth of the idler measured at FWHM, $W_{temp}(z)$ is the temporal walkoff between the pump and signal, $W_{spat}(z)$ is the spatial walkoff between the pump and signal, and z is the propagation distance measured in mm.

6 Experimental characterisation of Tm:Ho system

After the simulations presented in chapters 4 and 5 had been carried out, the Tm:Ho laser system from Menlo Systems was delivered to the Attoscience and Ultrafast Optics laboratory at the Institut of Photonic Sciences (ICFO). As discussed previously the broadband 1.5 μm arm is internally compressed and characterized. The broadband 2 μm arm on the other hand is a newly developed and unique source and therefore the pulse chirp is completely unknown. The aim of this chapter is to show the characterisation of this output and implement a compressor to obtain the minimum possible pulse duration. This has led to an international journal publication [53] (in submission) and an oral presentation at ASSP [53]. The measured performances differ minorly from the specified factory outputs - used in the simulation section - as will be seen in this section. The slight deviations in average power and spectrum will not alter any previous conclusion from Chap. 5.

6.1 Spectral and temporal characterisation of the 1.5 μm and 2 μm outputs

The spectra of the 1.5 μm pump and 2 μm signal broadband outputs are measured using a Fourier-transform IR spectrometer (FTIR) and are shown in Fig. 6.1. The pulses exhibit a spectrum of 130 nm and 81 nm of bandwidth at $1/e^2$ for the pump pulses and signal pulses respectively. The centre of gravity of the pulses is computed and found to be 1.56 μm and 2.05 μm , yielding a transform limit of 40 fs and 130 fs for the pump and signal respectively. The average power at the output of the Tm:Ho system was measured to be 360 mW and 320 mW for the pump and signal respectively, which at the repetition rate of 100 MHz yields pulse energies of 3.6 nJ and 3.2 nJ.

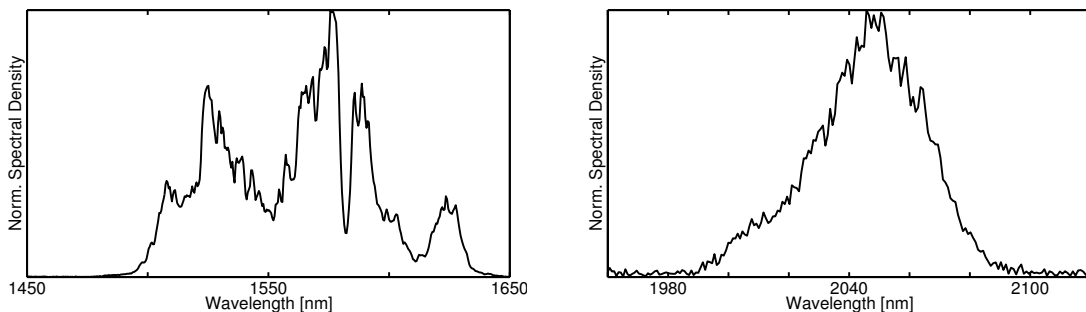


Figure 6.1: Spectra of the input pulses for the DFG stage measured at ICFO: (left) 1.55 μm broadband pulse and (right) 2.05 μm broadband signal

As discussed previously the pump output at 1.5 μm is internally compressed in the

Tm:Ho system. The pulse duration is measured with SH-FROG [50] featuring a 250 μm BBO crystal and reveals a pulse duration of 72 fs with a FROG error $<0.2\%$. The setup for the FROG is shown in Fig. 6.2, the detector in this case is a spectrometer. The FROG retrieved pulse duration, instantaneous frequency, spectrum and spectral phase are shown in Fig. 6.3.

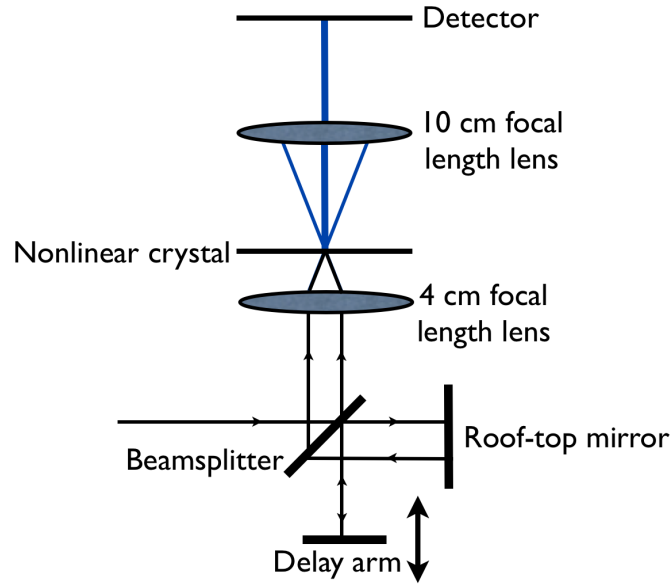


Figure 6.2: Setup for the autocorrelator and SH-FROG.

As a first approach, the pulse duration of the 2 μm output is characterized through an intensity autocorrelation, which is carried out using the same setup as the one described above, using a photodiode as the detector. The reason for using noncollinear geometry is to obtain angular separation of the sum-frequency signal arising from the overlapped pulses from the second harmonic signal arising from each pulse. Obtaining a signal from the nonlinear interaction proves to be challenging in the case of the 2 μm output due to the necessity of finding a nonlinear crystal transparent at 2 μm with a sufficiently high nonlinearity to generate a measurable second harmonic signal for a pulse with a duration in the ps range, and therefore low peak intensity. As a first attempt, polychristalline ZnSe is used due to its ability to phase match a wide variety of bandwidths and angles [49]. A thin 3 mm piece is used as the nonlinear crystal shown in Fig 6.2. Using this setup a sum-frequency signal is obtained allowing us to obtain an intensity autocorrelation measurement. The autocorrelation reveals a pulse duration of approximately 30 ps. In order to fully characterize the pulses, SH-FROG with noncollinear geometry is used. The setup is identical to the one shown in Fig 6.2. Due to interference patterns in the generated spectrum, ZnSe was shown to be unsuitable for this purpose. Subsequently a 250 μm crystal of barium borate (BBO) is used. BBO has a transparency range up to approximately 2 μm but proves suitable for second harmonic generation for the signal pulse.

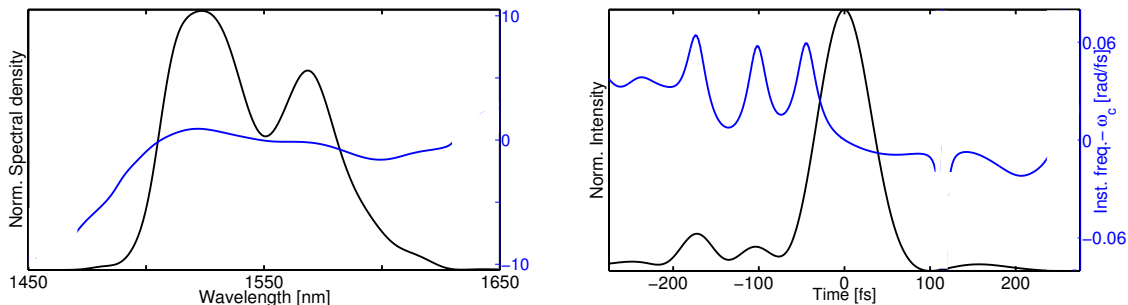


Figure 6.3: FROG results for the 1.5 μm output. (Left) Temporal profile and instantaneous frequency retrieved by the FROG algorithm. (Right) Retrieved spectrum and spectral phase of the compressed pulses.

The signal pulse is measured and reveals a pulse duration of 25 ps with a FROG error $<2\%$. The pulse duration, instantaneous frequency, spectrum and spectral phase are shown in Fig. 6.4. The pulse presents a large second order spectral phase, but due to the intrinsic time-reversal ambiguity in the SH-FROG measurement, the sign of the chirp is unknown. Nevertheless, the chirp of the signal pulse is estimated through the effect of dispersion in the nonlinear fibre, and due to the long wavelength, it is assumed that the dispersion is in the anomalous regime and thus the sign of the chirp is expected to be negative.

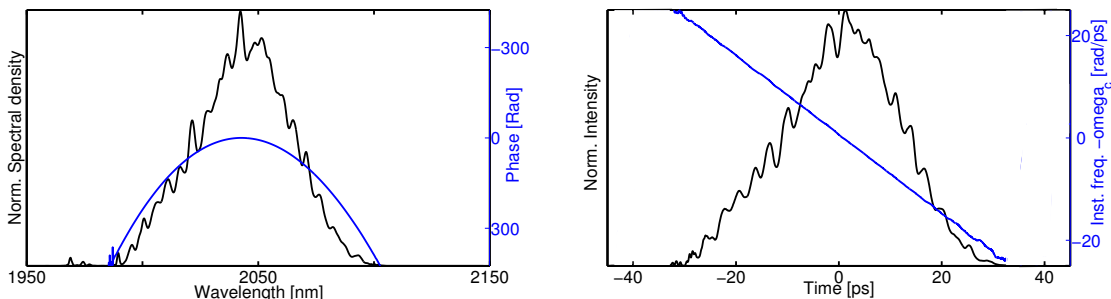


Figure 6.4: FROG results for the uncompressed 2 μm output. (Left) Temporal profile and instantaneous frequency retrieved by the FROG algorithm. (Right) Retrieved spectrum and spectral phase of the compressed pulses.

6.2 Compression of the 2 μm broadband output

As shown in Chap. 2, DFG is an intensity driven process and high peak power for the input pulses is required in order for the process to be efficient. Therefore it is necessary to temporally compress the 2 μm broadband pulse to the fs regime before the DFG stage. Taking in to account the results from the SH-FROG measurement carried out in the previous section, a Martinez-type compressor [51] is designed. A free-space compressor using

a 30-cm-focal-length spherical gold mirror, gold reflective optics and an aluminium coated diffraction grating with 360 lines/mm is built and used to compress the chirped pulses. The setup of the compressor is depicted in Fig. 6.5. The compressor assembly was adjusted to ensure optimum third order dispersion (TOD) compensation and eliminate spatial chirp.

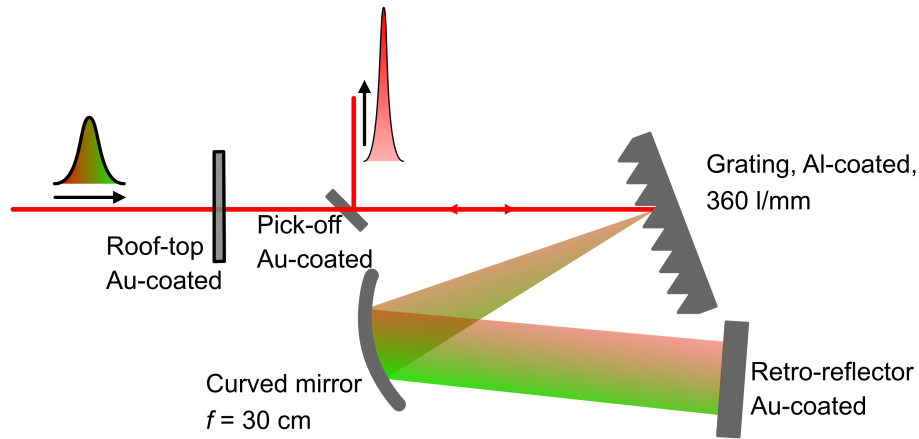


Figure 6.5: Setup of the Martinez-style compressor

The compressed pulses are characterized with the same SH-FROG setup described above. The retrieved pulse in both temporal and spectral domain are shown in Fig. 6.6. The FROG error is $<0.15\%$. Due to losses in the grating, the output beam after compression presents an average power of 55 mW, which gives an overall transmission of 20%. The measured pulse duration after compression is 135 fs, which is 96% of the transform limit.

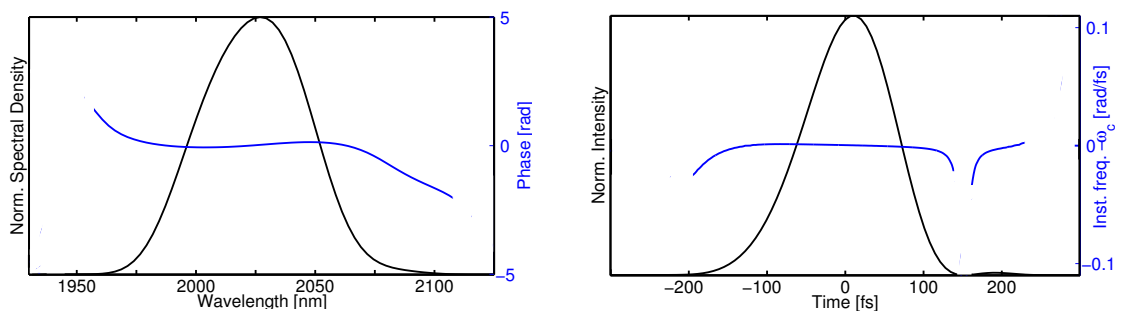


Figure 6.6: FROG results for the compresses $2\ \mu\text{M}$ output. (Left) Temporal profile and instantaneous frequency retrieved by the FROG. (Right) Retrieved spectrum and spectral phase of the compressed pulses.

7 Conclusion and future work

To conclude, we have designed a DFG stage for delivering intrinsically few-cycle CEP stable pulses centred at $7\ \mu\text{m}$ to seed an OPCPA chain. The generated spectrum is designed to support a minimum Fourier transform limit of 40 fs, which is a less than 2 optical cycles. The nonlinear crystal chosen for the parametric downconversion process is cadmium silica phosphate (CdSiP_2 or CSP). CSP is a newly developed nonlinear crystal with unique properties that outperforms the other mid-IR materials available. In order to design the DFG stage and choose the nonlinear material, the theoretical aspects of DFG were presented and discussed in Chap. 2. In Chap. 3, a review of the nonlinear crystals available for the mid-IR spectral range was presented and the suitability of the crystals for the DFG stage was discussed. A simple numerical evaluation of the analytical solutions was used in Chap. 4 to obtain a first approximation estimate of the phase matching abilities of the nonlinear crystals under consideration. In Chap. 5 the full 3D nonlinear propagation code Sisyfos was used to simulate the DFG process in order to exhaustively study the performance of the crystals. Finally, in Chap. 6 the temporal and spectral characterisation of the input pulses for the DFG stage was shown and a compressor for the $2\ \mu\text{m}$ output was designed and implemented.

Future work will focus on the design and construction of the mid-IR OPCPA system, which includes as a first step the experimental implementation of the DFG stage described in this thesis. Subsequently, the 3D nonlinear code will be used to design and choose the crystal for the OPA stages which will be used to amplify the $7\ \mu\text{m}$ seed pulse created in the DFG stage.

A APPENDIX - SELLMEIER COEFFICIENTS

For future reference, the Sellmeier equations used throughout the thesis are shown here. All the wavelengths are measured in μm .

AGS [41]:

$$n_o^2 = 5.7975 + \frac{0.2311}{\lambda^2 - 0.0688} - 0.00257\lambda^2$$

$$n_e^2 = 5.5436 + \frac{0.2230}{\lambda^2 - 0.0946} - 0.00261\lambda^2$$

AGSe [42]:

$$n_o^2 = 6.849065 + \frac{0.417863}{\lambda^{1.970203} - 0.178080} + \frac{0.000442}{\lambda^{0.340086} - 0.889242} + \frac{1.209374}{1 - 915.345/\lambda^{1.921292}}$$

$$n_e^2 = 6.675232 + \frac{0.436579}{\lambda^{1.893694} - 0.229775} + \frac{0.012063}{\lambda^{4.269152} - 0.213957} + \frac{3.252722}{1 - 3129.32/\lambda^{2.047204}}$$

CSP [43]:

$$n_o^2 = 3.72202 + \frac{5.91985\lambda^2}{\lambda^2 - 0.06408} - \frac{3.92371\lambda^2}{\lambda^2 - 2071.59}$$

$$n_e^2 = 4.77331 + \frac{4.77331\lambda^2}{\lambda^2 - 0.08006} - \frac{0.91879\lambda^2}{\lambda^2 - 496.71}$$

GS [44]:

$$n_o^2 = 7.443 + \frac{0.4050}{\lambda^2} + \frac{0.0186}{\lambda^4} + \frac{0.0061}{\lambda^6} + \frac{3.1485\lambda^2}{\lambda^2 - 2194}$$

$$n_e^2 = 5.760 + \frac{0.3879}{\lambda^2} + \frac{-0.2288}{\lambda^4} + \frac{0.1223}{\lambda^6} + \frac{1.855\lambda^2}{\lambda^2 - 1780}$$

LGS [38]:

$$n_x^2 = 4.326834 + \frac{0.1030907}{\lambda^2 - 0.0309876} - 0.0037015\lambda^2$$

$$n_y^2 = 4.478907 + \frac{0.120426}{\lambda^2 - 0.034616} - 0.0035119\lambda^2$$

$$n_z^2 = 4.493881 + \frac{0.1177452}{\lambda^2 - 0.0337004} - 0.0037767\lambda^2$$

LGS_e [38]:

$$n_x^2 = 4.99592 + \frac{0.1513}{\lambda^2 - 0.08989} - 0.00233\lambda^2$$

$$n_y^2 = 5.20896 + \frac{0.18632}{\lambda^2 - 0.07687} - 0.00211\lambda^2$$

$$n_z^2 = 5.22442 + \frac{0.18365}{\lambda^2 - 0.07493} - 0.00232\lambda^2$$

LIS [45]:

$$\begin{aligned}
n_x^2 &= 6.686059 + \frac{0.1385833}{\lambda^2 - 0.05910334} - \frac{2047.46509}{\lambda^2 - 897.7476} \\
n_y^2 &= 7.095493 + \frac{0.1422326}{\lambda^2 - 0.06614640} - \frac{2511.08936}{\lambda^2 - 988.2024} \\
n_z^2 &= 7.256327 + \frac{0.15072}{\lambda^2 - 0.06823652} - \frac{2626.10840}{\lambda^2 - 983.0503}
\end{aligned}$$

LISe [46]:

$$\begin{aligned}
n_x^2 &= 5.669848 + \frac{0.1948525}{\lambda^2 - 0.09473786} - \frac{300.72708}{\lambda^2 - 492.0924} \\
n_y^2 &= 5.676208 + \frac{0.2451579}{\lambda^2 - 0.06265155} - \frac{205.05597}{\lambda^2 - 432.8862} \\
n_z^2 &= 6.302234 + \frac{0.2509052}{\lambda^2 - 0.04137438} - \frac{755.68622}{\lambda^2 - 713.0767}
\end{aligned}$$

Bibliography

- [1] T. Popmintchev, M. C. Chen, A. Bahabad, M. Gerrity, P. Sidorenko, O. Cohen, I. P. Christov, M. M. Murnane, and H. C. Kapteyn, "Phase matching of high harmonic generation in the soft and hard X-ray regions of the spectrum," *Proc. Natl. Acad. Sci. USA* **106**, 10516-10521 (2009).
- [2] B. Jean and T. Bende, "Mid-IR laser applications in medicine," *Topics in Applied Physics* **89**, 530-565 (2003).
- [3] G. Renz and W. Bohn, *Proc. SPIE* 6552, 655202 (2007).
- [4] A. D. DiChiara, S. Ghimire, C. I. Baga, E. Sistrunk, E. P. Power, A. M. March, T. A. Miller, D. A. Reis, P. Agostini, and L. F. DiMauro, "Scaling of high-order harmonic generation in the long wavelength limit of a strong laser field," *IEEE J. Sel. Top. Quantum Electron.* **18**, 419-433 (2012).
- [5] C. Hernandez-Garcia, J. A. Perez-Hernandez, T. Popmintchev, M. M. Murnane, H. C. Kapteyn, A. Becker, and L. Plaja, "Zeptosecond High Harmonic keV X-Ray Waveforms Driven by Midinfrared Laser Pulses," *Phys. Rev. Lett.* **111**, 033002 (2013).
- [6] O. Chalus, P. Bates, M. Smolarski, J. Biegert, "Mid-IR short-pulse OPCPA with micro-Joule energy at 100 kHz", *Opt. Exp.* **17**, 3587-3594, (2009).
- [7] C. Erny, C. Heese, M. Haag, L. Gallmann, and U. Keller, "High-repetition-rate optical parametric chirped-pulse amplifier producing 1- μ J, sub-100-fs pulses in the mid-infrared," *Opt. Express* **17**, 1340 (2009).
- [8] G. Andriukaitis, T. Balciunas, S. Alisauskas, A. Pugzlys, A. Baltuska, T. Popmintchev, M. C. Chen, M. M. Murnane, and H. C. Kapteyn, "90 GW peak power few-cycle mid-infrared pulses from an optical parametric amplifier," *Opt. Lett.* **36**, 2755 (2011).
- [9] V. Petrov, "Parametric down-conversion devices: The coverage of the mid-infrared spectral range by solid-state laser sources," *Optical Materials* **34**, 536-554 (2012).
- [10] R. W. Boyd, *Nonlinear Optics*, Third edition, AP, New York, 2008.
- [11] Y. R. Shen, *The principle of Nonlinear Optics*, Wiley Classics, 2002.
- [12] J. A. Armstrong, N. Bloembergen, J. Ducuing, and P. S. Pershan, "Interactions between light waves in a nonlinear dielectric," *Physical Review* **127**, 1918 (1962).
- [13] R. A. Baumgartner, and R. L. Byer, "Optical parametric amplification," *IEEE Journal of Quantum Electronics* **15**, 432 (1979).
- [14] I. N. Ross, P. Matousek, G. H. C. New, and K. Osvay, "Analysis and optimization of optical parametric chirped pulse amplification," *Journal of the Optical Society of America B* **19**, 2945-2957 (2002).
- [15] A. Shirakawa *et al.*, "Sub-5-fs visible pulse generation by pulse-front-matched noncollinear optical parametric amplification", *Appl. Phys. Lett.* **74** (16), 2268 (1999).
- [16] D. N. Schimpf *et al.*, "Theoretical analysis of the gain bandwidth for noncollinear parametric amplification of ultrafast pulse", *J. Opt. Soc. Am. B* **24** (11), 2837 (2007).
- [17] F. Krausz and M. Ivanov, "Attosecond physics," *Rev. Mod. Phys.* **81**, 163 (2009).

- [18] E. Goulielmakis, M. Schultze, M. Hofstetter, V. S. Yakovlev, J. Gagnon, M. Uiberacker, A. L. Aquila, E. M. Gullikson, D. T. Attwood, R. Kienberger, F. Krausz, and U. Kleineberg, "Single-cycle nonlinear optics" *Science* **20**, 1614-1617 (2008).
- [19] Y. S. Lee, J. H. Sung, C. H. Nam, T. J. Yu, and K.-H. Hong, "Novel method for carrier-envelope phase stabilization of femtosecond laser pulses," *Opt. Express* **13**, 2969-2976 (2005).
- [20] S. Koke, C. Grebing, H. Frei, A. Anderson, A. Assion, and G. Steinmeyer, "Direct frequency comb synthesis with arbitrary offset and shot-noise limited phase noise," *Nat. Photonics* **4**, 462-465 (2005).
- [21] G. Arisholm and H. Fonnum, Operating manual for Sisyfos, 2011.
- [22] K.F.Hulme, O.Jones, P.H.Davies, M.V.Hobden, "Synthetic proustite: a new crystal for optical mixing," *Appl. Phys. Lett.* **10** (4), 133-135 (1967).
- [23] D. C. Hanna, V. V. Rampal, and R. C. Smith, "Tunable infrared down-conversion in silver thiogallate," *Opt. Commun.* **8**, 151- 153 (1973).
- [24] R.L. Byer, M.M. Choy, R.L. Herbst, D.S. Chemla, R.S. Feigelson, "Second harmonic generation and infrared mixing in AGSe," *Appl. Phys. Lett.* **24**(2), 65-68 (1974).
- [25] H.P. Chou, R.C. Slater, Y. Wang, "High-energy, fourth-harmonic generation using CO₂ lasers," *Appl. Phys. B* **66**(5), 555-559 (1998).
- [26] G.D. Boyd, E. Buehler, F.G. Storz, "Linear and nonlinear optical properties of ZnGeP₂ and CdSe," *Appl. Phys. Lett.* **18**(7), 301-304 (1971).
- [27] R.L.Byer, H.Kildal, R.S.Feigelson, "CdGeAs₂-a new non linear crystal phase matchable at 10.6 μm ," *Appl. Phys. Lett.* **19**(7), 237-240 (1971).
- [28] K.L. Vodopyanov, P.G. Schunemann, "Broadly tunable noncritically phase-matched ZnGeP₂ optical parametric oscillator with a 2 μmJ pump threshold. *Opt. Lett.* **28**(6), 441- 443 (2003).
- [29] E. Tanaka, K. Kato, "Second-harmonic and sum-frequency generation in CdGeAs₂," *MRS Symposium Proceedings*, Vol. 384, *Infrared Applications of Semiconductors II*, ed by D.L. McDaniel, Jr., M.O. Manasreh, R.H. Miles, S. Sivananthan (Materials Research Society, Warrendale, PA, 1998), pp. 475-479.
- [30] M.M. Choy, R.L. Byer, "Accurate second-order susceptibility measurements of visible and infrared nonlinear crystals. *Phys. Rev. B* **14**(4), 1693-1706 (1976).
- [31] L. Kador, D. Haarer, K.R. Allakhverdiev, E.Y. Salaev, "Phase-matched second-harmonic generation at 789.5 nm in a GaSe crystal," *Appl. Phys. Lett.* **69**(6), 731-733 (1996).
- [32] D. Haertle, M. Jazbinsek, G. Montemezzani, P. Gunter, "Nonlinear optical coefficients and phase-matching conditions in Sn₂P₂S₆," *Opt. Express* **13** (2005) 3765.
- [33] M. D. Ewbank, P. R. Newman, N. L. Mota, S. M. Lee, W. L. Wolfe, "The temperature dependence of optical and mechanical properties of Tl₃AsSe₃," *J. Appl. Phys.* **51**, 3848 (1980).
- [34] V. V. Badikov, A. G. Tyulyupa, G. S. Shevyrdyaeva, and S. G. Sheina, "Solid solutions in the AgGaS₂-GeS₂ and AgGaSe₂-GeSe₂ systems," *Inorg. Mater.* **27**, 177-180 (1991).
- [35] B.F. Levine, C.G. Bethea, H.M. Kasper, F.A. Thiel, "Nonlinear optical susceptibilities of HgGa₂S₄," *IEEE J. Quant. Electr.* **12**(6), 367-368 (1976).
- [36] V.V. Badikov, A.K. Don, K.V. Mitin, A.M. Seregin, V.V. Sinaiskii, N.I. Shchebetova, "A HgGa₂S₄ optical parametric oscillator," *Kvant. Elektron.* **33**(9), 831-832 (2003) [In Russian, English trans.: *Quantum Electron.* **33**(9), 831-832 (2003).

- [37] V. Petrov, P. G. Schunemann, K. T. Zawilski, and T. M. Pollak, "Noncritical singly resonant optical parametric oscillator operation near $6.2 \mu\text{m}$ based on a CdSiP₂ crystal pumped at 1064 nm," *Opt. Lett.* **34**, 2399 (2009).
- [38] V. Petrov, A. Yelisseyev, L. Isaenko, S. Lobanov, A. Titov, and J.-J. Zondy, "Second harmonic generation and optical parametric amplification in the mid-IR with orthorhombic biaxial crystals LiGaS₂ and LiGaSe₂," *Appl. Phys. B* **78**, 543-546 (2004).
- [39] L. Isaenko, A. Yelisseyev, S. Lobanov, V. Petrov, F. Rotermund, J.-J. Zondy, G.H.M. Knippels, "LiInS₂: a new nonlinear crystal for the mid-IR," *J. Mater. Sci. Semicond. Process.* **4**(6), 665-668 (2002).
- [40] L. Isaenko, A. Yelisseyev, S. Lobanov, V. Petrov, F. Rotermund, G. Sleky, J.-J. Zondy, "LiInSe₂: a biaxial ternary chalcogenide crystal for nonlinear optical applications in mid-infrared," *J. Appl. Phys.* **91**(12), 9475-9480 (2002).
- [41] E. Takaoka, K. Kato, "Thermo-optic dispersion formula for AgGaS₂," *Appl. Opt.* **38**, 4577 (1999).
- [42] D. A. Roberts, "Dispersion equations for nonlinear optical crystals: KDP, AgGaSe₂, and AgGaS₂," *Appl. Opt.* **35**, 4677 (1996).
- [43] V. Kemlin, P. Brand, B. Boulanger, P. Segonds, P. G. Schunemann, K. Zawilski, B. Menaert, J. Debray, "Thermo-optic dispersion formula for AgGaS₂," *Opt. Lett.* **36**, 1800 (2011).
- [44] K.L. Vodopyanov, L.A. Kulevskii, "New dispersion relationships for GaSe in the 0.65-18 μm spectral region," *Opt. Comm.* **118**, 375 (1995).
- [45] Fossier *et al*, "Optical, vibrational, thermal, electrical, damage, and phase-matching properties of lithium thioindate," *J. Opt. Soc. Am. B.* **21**, 1981 (2004).
- [46] Petrov *et al*, "Optical, thermal, electrical, damage, and phase-matching properties of lithium selenoindate," *J. Opt. Soc. Am. B.* **27**, 1902 (2010).
- [47] G. Arisholm, "General numerical methods for simulating second-order nonlinear interactions in birefringent media," *J. Opt. Soc. Am. B* **14**, 2543 (1997).
- [48] C. P. Hauri, P. Schlup, G. Arisholm, J. Biegert, and U. Keller, "Phase-preserving chirped-pulse optical parametric amplification to 17.3 fs directly from a Ti:sapphire oscillator," *Opt. Lett.* **29**, 1369 (2004).
- [49] E. Sorokin, I. T. Sorokina, "Femtosecond Operation and Random Quasi-Phase-Matched Self-Doubling of Ceramic Cr:ZnSe Laser," Conference on Lasers and Electro-Optics, CLEO 2010, May 16-21, San Jose (CA), USA.
- [50] D. J. Kane, R. Trebino, "Single-shot measurement of the intensity and phase of an arbitrary ultrashort pulse by using frequency-resolved optical gating," *Opt. Lett.* **18**, 823-825 (1993).
- [51] O. E. Martinez, J. P. Gordon, and R. L. Fork, "Negative group-velocity dispersion using refraction," *J. Opt. Soc. Am. A* **1**, 1003-1006 (1984).
- [52] Heinar Hoogland, Alexandre Thai, Martin Engelbrecht, Jens Biegert, Ronald Holzwarth, "All-PM coherent 2.05 μm Thulium/Holmium fiber frequency comb source with broadband and narrowband pulses at 100 MHz and up to 0.5 W average power," in proceedings of MICS, Paris (2013).
- [53] H. Hoogland, A. Thai, D. Sanchez, S. Cousin, M. Hemmer, M. Engelbrecht, J. Biegert, R. Holzwarth, "All-PM coherent 2.05 μm Thulium/Holmium fiber frequency comb source at 100 MHz with up to 0.5 W average power and pulse duration down to 135 fs," Submitted to *Opt. Expr.* (August, 2013).